# AN ALGORITHM FOR RETRIEVAL OF OPTICAL PROPERTIES, BATHYMETRY AND BENTHIC COVER IN SHALLOW WATERS FROM HYPERSPECTRAL IMAGERY

By

Alexey Castrodad Carrau

A thesis submitted in partial fulfillment of the requirements for the degree of

MASTER OF SCIENCE
In

ELECTRICAL ENGINEERING
UNIVERSITY OF PUERTO RICO
MAYAGÜEZ CAMPUS
2005

Approved by:

| | |
|---|---|
| Miguel Vélez Reyes, Ph.D<br>President, Graduate Committee | Date |
| James A. Goodman, Ph.D<br>Member, Graduate Committee | Date |
| Shawn D. Hunt, Ph.D<br>Member, Graduate Committee | Date |
| Wilson Rivera, Ph.D<br>Member, Graduate Committee | Date |
| Fernando Gilbes, Ph.D<br>Representative of Graduate Studies | Date |
| Isidoro Couvertier, Ph.D<br>Chair ECE Department | Date |

# ABSTRACT

Hyperspectral imagery has been shown to be a powerful technology for quantitative monitoring of shallow water coastal environments. In coastal remote sensing, to estimate sea bottom properties from hyperspectral imagery, we need to remove the effects of the atmosphere and the water column from the measured spectral signature. In our work, we use a standard algorithm available from NRL to correct for atmospheric effects in hyperspectral imagery to retrieve the water leaving remote sensing reflectance, $\boldsymbol{R_{rs}}$, from which the subsurface remote sensing reflectance, $\boldsymbol{r_{rs}}$, is retrieved. Here, we present results in the development of an algorithm combining inversion and unmixing models to retrieve bottom reflectance, water column optical properties, bathymetry, and benthic composition from subsurface remote sensing reflectance. A bio-optical model developed by Z.P. Lee in 1998 and 1999 relates $\boldsymbol{R_{rs}}$ and $\boldsymbol{r_{rs}}$ to the water optical properties (OP's), depth, and bottom reflectance. We employ an iterative algorithm to retrieve the parameters of interest. As in Goodman (2004), Lee's original model is enhanced by adding a linear mixing model for approximating bottom composition, which is used to extract subpixel information in low spatial resolution satellite and airborne hyperspectral sensors. Results using both simulated data and AVIRIS imagery from Hawaii are presented.

## RESUMEN

Las imágenes hiperespectrales han demostrado ser una tecnología de gran alcance para el monitoreo cuantitativo de los ambientes costeros en aguas no profundas. Para estimar las características del fondo marino usando imágenes hiperespectrales, se necesita remover los efectos de la atmósfera y de la columna del agua de la firma espectral medida. En nuestro trabajo, utilizamos un algoritmo estándar de NRL para corregir por los efectos atmosféricos en imágenes hiperespectrales para recuperar la reflectancia de percepción remota en la superficie del agua, $\boldsymbol{R_{rs}}$, y de la cual se puede obtener la reflectancia subsuperficial de percepción remota del agua, $\boldsymbol{r_{rs}}$. Aquí, presentamos resultados en el desarrollo de un algoritmo que combina inversión y separación espectral aproximando la reflectancia subsuperficial de percepción remota para extraer características ópticas de la columna de agua, batimetría y composición béntica. Un modelo bio-óptico desarrollado por Z.P. Lee en 1998 y 1999 relaciona la $\boldsymbol{R_{rs}}$ y $\boldsymbol{r_{rs}}$ con las propiedades ópticas (P.O.s) de la columna de agua y del fondo es utilizado. Empleamos un algoritmo iterativo para obtener los parámetros de interés. De manera similar a Goodman (2004), el modelo de Lee es mejorado agregando un modelo de mezclado espectral lineal para aproximar la composición béntica del fondo marino, el cual es usado para extraer información a nivel de subpixel y compensar por la baja resolución espacial en sensores hiperespectrales en satélites y aviones. Se presentan resultados usando datos simulados e imágenes de AVIRIS sobre Hawaii.

# DEDICATION

*To the Lord, for giving me the energy to overcome every difficult moment.*

*To my parents, for their unconditional love and support, and for sharing with me all my achievements.*

## ACKNOWLEDGMENTS

I want to thank Dr. Miguel Vélez Reyes for his faith in me, guidance, patience and incomparable wisdom. To Dr. James Ansell Goodman for his long hours spent with me, his expertise, goodwill, and for providing me with the Kaneohe Bay AVIRIS data and the SHOALS data from that area. To my committee members: Dr. Shawn Hunt and Dr. Wilson Rivera for helping me with this work.

Also very special thanks to all the crew in LARSIP and CenSSIS: Emmanuel, Samuel, Rosa, Marie, Claribel, Maribel and Carmen Vanessa.

This work was supported in part by CenSSIS, the Center for Subsurface Sensing and Imaging Systems, under the Engineering Research Centers Program of the National Science Foundation (Award Number EEC-9986821).

# TABLE OF CONTENTS

# LIST OF FIGURES

# LIST OF TABLES

# Chapter 1

# Introduction

## 1.1 Justification

Coral reefs play a very important role in our planet. Their importance is measured by means of ecological, economical, and social value. Among the benefits that coral reefs provide are the protection of other associated ecosystems, prevention of erosion and flooding, a rich source of marine species, and a fishing and tourist attraction. Coral reefs have been declining in recent years. For instance, coral bleaching may be attributed to an increase in water temperature [18], causing them to lose almost all of their symbiotic zooxanthellae, containing much of the pigmentation. Contamination, sedimentation rates, over-fishing, dredging to make ship channels are just a few of the anthropogenic factors affecting coral reefs [18, 19]. For that reason, there is a need for protecting and preserving these ecosystems, thus requiring a quantitative method for monitoring them. Such an approach can be provided by remote sensing and image analysis.

Remote sensing can be used as a method for assessing and monitoring coral reefs. Analysis using multispectral sensors such as Landsat and IKONOS are available [20, 22, 23], but effectiveness using this data has been limited due to the low spectral information of these instruments (i.e. relatively broad wavelength bands or channels), which are insufficient for a detailed benthic classification.

**Figure 1.1** Coral Reefs. From www.nmfs.noaa.gov

Usually, simplifying assumptions, *in situ* data or spectral libraries extracted from hyperspectral sensors must be used to compensate for the low spectral resolution. Purkis [20] integrated *in situ* reef reflectance spectra with Landsat imagery, and used known depths on the area of study to obtain reasonable results. In other study [22], Zhang combined Landsat and SAR data to study optically denseity in shallow waters at the Gulf of Finland. Mishra [23] simplified a bio-optical model for retrieving bathymetry to adapt it to multispectral IKONOS, and obtained good classification results. Purkis also have conducted coral reef habitat classifications from IKONOS imagery. He used a classifier trained with statistics down-sampled from hyperspectral data. Although some of these studies have obtained satisfactory results, one can observe that a detailed spectral analysis of each pixel is not possible. Multispectral information stands short when there is need to know a detailed assessment of the components in each pixel. That is one of the most important features that can be extracted when high spectral resolution is available. Hyperspectral technology allows us to extract multiple layer of information from a complex optical signal can be extracted providing the necessary information for identifying the fractional contribution of classes or endmembers that relate to actual components in the study area in both a spatial and temporal way. As a simple example, assuming that coral reef and other benthic habitats can be subdivided into live coral, sea-grass and sand, an image can be classified in order to obtain a spatial indication of variations in these three main reef components [1]. It is important to mention that combination of other endmembers is possible. Temporal changes may be obtained through the observation of different classification results over a sequence of images over time. For example, changes of classifications from the same area may indicate a loss of coral and an increase of algae, or vice versa. The work presented here combines two existing models into a single algorithm for estimating the optical properties of the water, bathymetry, bottom albedo and benthic habitat classification from hyperspectral imagery.

## 1.2 Problem Statement

The estimation of water optical properties, bathymetry, and bottom characteristics from remote sensing imagery is important in order to facilitate the monitoring of benthic habitats, including coral reefs. Inherent Optical properties (IOP) specify the optical attributes of natural water that depend only on the medium, thus independent of the ambient light field. The most studied IOP's are the absorption and backscattering coefficients. Apparent Optical properties (AOP) are dependant on the ambient medium and on the geometric (directional) structure of the ambient light field (e.g. remote sensing reflectance) [2, 3].

The problem of extracting these optical properties (OP) is difficult since there are many energy interactions affecting a given scene. Usually, the hyperspectral sensor uses sunlight as the light source. When it receives the signal, it is mixed with atmospheric radiance, sea surface reflection, scattering from the water, and bottom reflectance. The scattering from the water depends on the different particles, phytoplankton and other types of matter that describe the water column. So, the bottom reflectance received is highly correlated to all these different contributions. Figure 1.2 illustrates this problem.

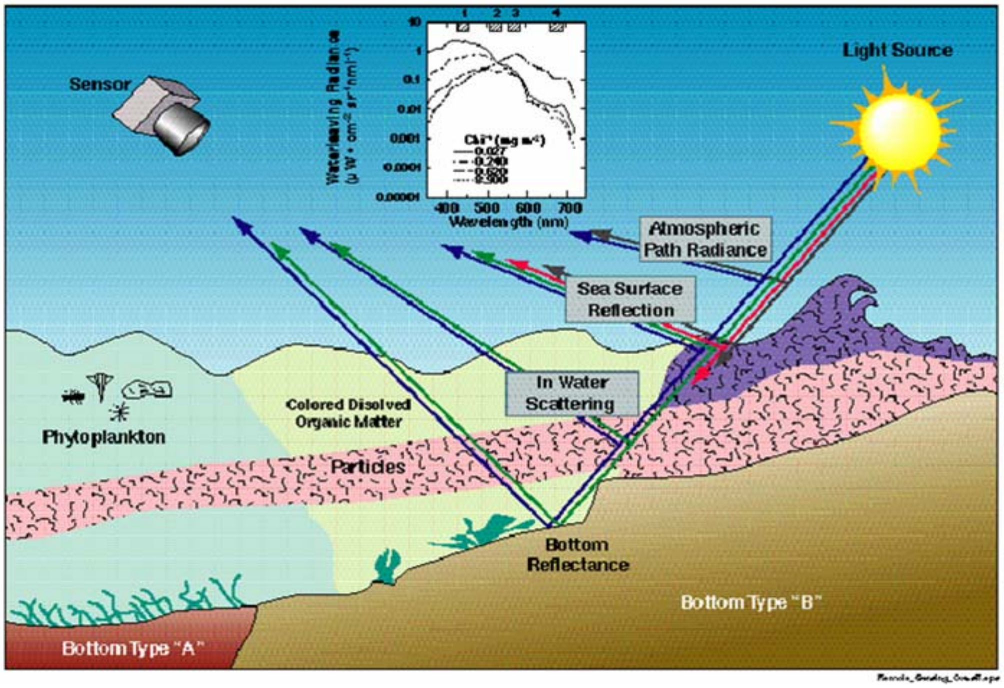


**Figure 1.2.** Energy interactions [1].

A system for the extraction of the IOP's and the bottom reflectance is described in Figure 1.3. If measured remote sensing reflectance is taken as the input, the IOP's are estimated by minimizing the difference between the measured and the output of a semi-analytical model relating IOP's and bathymetry with remote sensing reflectance.

The proposed algorithm consists of

1. The application of a bio-optical model as described by Lee [4].
2. Parameter estimation of the water and bottom properties via optimization and the use of linear unmixing for extracting the bottom reflectance similar to that of Goodman [1].

[1] from C.O. Davis Hyperspectral Imaging of the Littoral Battle Space, NRL Code 7203.

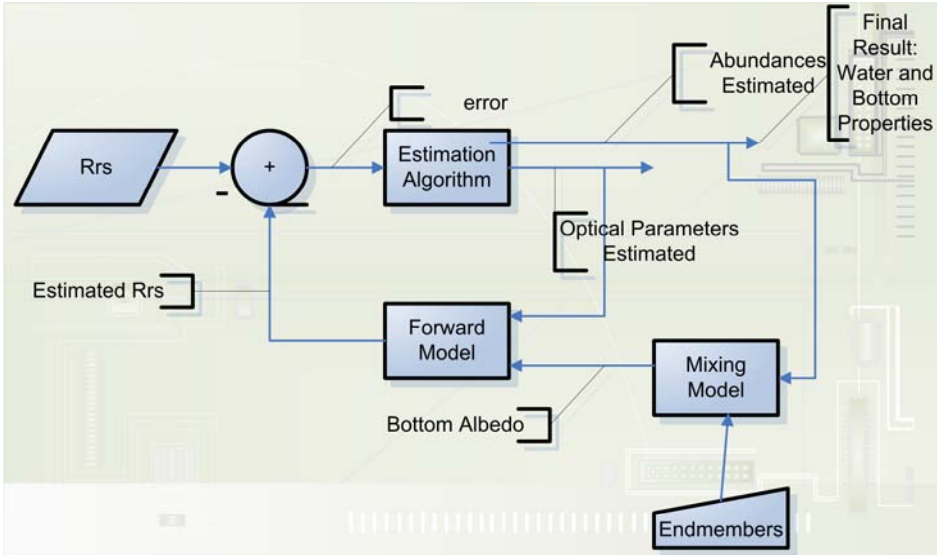


**Figure 1.3.** Water and Bottom Properties Estimation System

Figure 1.3 shows how the remote sensing reflectance obtained from the sensor is passed through the retrieval algorithm to obtain the water optical properties and the abundances for coral, sand, and algae. A final result would be the water and bottom properties obtained at convergence.

## 1.3 Objectives

There are three primary objectives of this work were to

- Implement an inversion algorithm and unmixing model to estimate optical properties and bottom reflectance from hyperspectral imagery of coastal environment.
- Evaluate and validate the algorithms with simulated and real data.
- Apply the developed algorithm to the problem of benthic habitat classification from remote sensing imagery.

Hyperspectral imagery of Kaneohe Bay, Hawaii was used as the primary test data to validate the advantages of hyperspectral remote sensing technology for the mapping and monitoring of benthic habitats. Water properties, bathymetry as well as sand, coral and algae fractional abundances were extracted from this data. Comparisons with measured bathymetry and results of Goodman [1] from the same site were used to test and validate the combined algorithms.

## 1.4 Contribution of this work

In this thesis we develop a new technique to simultaneously retrieve optical properties, bathymetry and bottom composition that can be used for the analysis of coral ecosystems and coastal environments. It shows the implementation of a semi-analytical model to retrieve bathymetry and optical properties of water from hyperspectral imagery, in combination with a linear unmixing algorithm for the classification of benthic habitats, considering the varying effects of the water column optical properties and bathymetry. The algorithms were validated for accuracy, using both synthetic and real data, and comparing water depth estimates with measurements from the Scanning Hydrographic Operational Airborne Lidar Survey (SHOALS) at Kaneohe Bay. Also, it applies the new techniques to an image of Kaneohe Bay taken from the AVIRIS airborne hyperspectral sensor and extracts information on benthic composition and water depths. This research innovates in performing the linear unmixing at the bottom level, retrieving bathymetry and optical properties (e.g. IOP's and AOP's) and at the same time give an approximation of the bottom reflectance in terms of fractional abundances of sand, coral and algae. It is based in subsurface remote sensing reflectance rather than surface remote sensing reflectance, thus taking advantage of the partially linear structure of the fractional abundances and the nonlinearity of the optical properties.

Very good results were obtained with this new approach. Water depth estimates were very close to SHOALS measurements. Abundance estimates seemed to be more consistent to those obtained by Goodman [1] on AVIRIS pixels, giving validity to the algorithm's ability to characterize complex bottoms.

## 1.5 Thesis Outline

This thesis is organized as follows:

Chapter 2 gives the necessary background and theoretical information for treating the problem of benthic classification and optical properties retrieval. Lee's inversion model and Goodman's linear unmixing technique is also discussed as an algorithm. Chapter 3 discusses the new approaches developed during this research. Chapter 4 focuses on the validation of the developed algorithms with both synthetic and real data. Chapter 5 analyzes a coastal scene of a Hawaiian Island and presents the different results obtained, including a benthic classification. Chapter 6 states the conclusions and recommendations for future works.

# Chapter 2

# Background and Literature Review

## 2.1 Hyperspectral Imagery

Imaging spectrometers are instruments that measure photons (emitted or reflected) and its variation of energy over a portion of the electromagnetic field [21]. The reflected sunlight on a given material in the surface, scattered light from within the atmosphere and also emitted energy are measured by the airborne or space sensors. This data is measured and stored in hundreds of narrow adjacent bands, thus representing an approximation of a continuous spectrum and a basis for identifying a given material or mixture of materials. One useful way to observe is to plot the reflectance as a function of wavelength. Furthermore, an image is built by arranging these reflectance measurements sequentially on a spatial basis over a specified area. Depending on the characteristics of the hyperspectral sensor system and its location (height) with respect to the Earth's surface (i.e., height), factors like spatial resolution and scene variability directly affect the visualization of the image. One important advantage of hyperspectral imagery is that they are not necessarily limited to the visible spectrum of light (take a look at Figure 2.1). It may also cover the near infrared (NIR), the midwave infrared (MWIR) and the long wave infrared (LWIR).

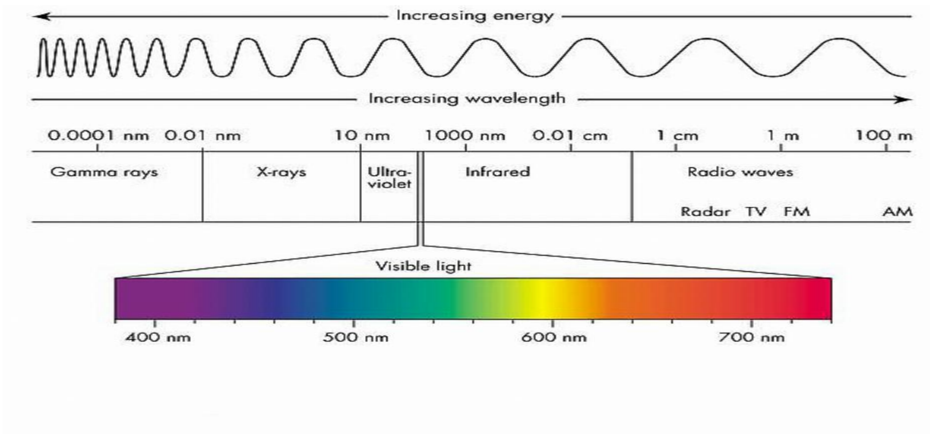


**Figure 2.1.** The Light Spectrum.

## 2.2 Hyperspectral Sensors

Next is a brief description of the AVIRIS and Hyperion remote sensors. Table 2.1 gives a summary of the instrument capabilities. Figure 2.2 gives a visual description of what a hyperspectral image consists of, naming the spectral bands, the spatial area, the pixels, and the cube itself.

*Airborne Visible/ Infrared Imaging Spectrometer (AVIRIS)*

AVIRIS is a 224-channel imaging spectrometer constructed by the Jet Propulsion Laboratory (JPL), and became fully operational in 1989. It covers the range 0.4 to 2.45 *μm* in 224 10-*nm*-wide contiguous bands. AVIRIS is typically on the NASA ER-2 aircraft at an altitude of 20 *km*, which produces approximately 20-*m* resolution per pixel and a 10.5-*km* swath width [27]. (Note: AVIRIS sensor can also be flown at other altitudes using the ER-2. The given specifications are appropriate for the data used in this work.)

*Hyperion*

NASA's Hyperion instrument acquires 242 spectral bands in the range 0.4 to 2.5 *μm* at 10-*nm* spectral resolution. However, not all 242 are useable. It is a spaceborn hyperspectral sensor with a 30-*m* spatial resolution and a swath width of 7.5-*km* at an altitude of 705-*km* [28].

**Table 2.1.** Hyperspectral sensor characteristics.

| | Spectral Resolution | Spectral Range | Spatial Resolution | Number of Bands |
|---|---|---|---|---|
| AVIRIS | 10*nm* | 0.4-2.45*μm* | 20*m* | 224 |
| Hyperion | 10*nm* | 0.4-2.5*μm* | 30*m* | 242 |

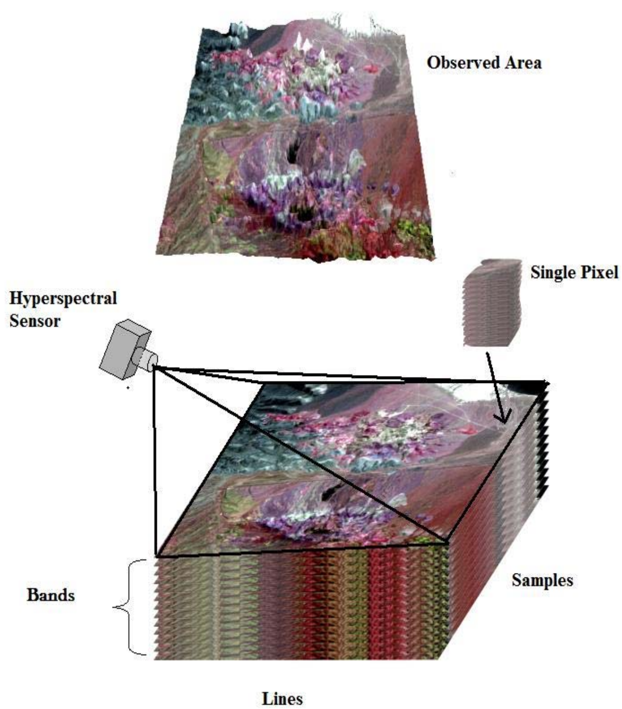


**Figure 2.2.** A better understanding of hyperspectral imagery.

## 2.3 Remote Sensing in Coastal Environments

Optically shallow waters are typically highly heterogeneous environments that experience a variety of dynamic processes which alter their optical properties. The signals measured by a sensor from above the water surface of a shallow site contain surface-reflected skylight, atmospheric skylight, radiance reflected from the bottom, and path radiance from the water column [4]. To retrieve the bottom albedo, the surface-reflected light and the water column contributions have to be removed, and the optical properties of the water column have to be known or derived.

In the past, water-column contributions were normally derived from adjacent deep waters while light attenuation properties were assumed to be known or derived empirically from an image. These assumptions are not necessarily correct since the path radiance from deep waters is not the same as that from the water column of shallow waters. Also, color constituents from deep waters are not homogeneous throughout an image, so the optical properties may not be the same. Moreover, due to the tidal influence, coastal water properties change fast and known depths are not always available for deriving regression parameters [4]. These constraints make attractive to derive concurrently the optical properties of the water column, bottom depths and albedo.

Several algorithms have been developed for the estimation of optical properties of the water and bottom. Taking advantage of the high spectral resolution of hyperspectral imagery, researchers like Maritorena [5] derived an equation that relates the reflectance just below the surface with the reflectance of the water column (without the bottom), the albedo, and the water depth with the assumption that the bottom is uniform. This approach, although more complex than an empirical relationship, does not resolve all the variables of interest. Also, one needs an estimate of two of the three parameters, to be able to calculate the third [1], or as in other studies where some OP's or water depths have to be supplied [6]. This kind of modeling as presented in [6] requires the use of either bathymetric charts or *in situ* data.

Different methods for the implementation of these models have been made to retrieve bathymetry and bottom composition from Hyperpspectral sensors [7, 8, 9, 6, 10]. For example, neural networks were used in [7]. Although these neural networks provide a robust implementation for obtaining bathymetry, they usually require a high amount of training data. Cluster analysis has also proven to give good results in the evaluation of the influence of water depth and bottom type in terms of downwelling irradiance and upwelling radiance as seen in [6]. Cluster analysis allowed for the isolation of anomalous behavior of light in the water column, with the help of a large database of *in situ* measures. Minimum Distance classifiers were used in [8], to successfully discriminate between two sea-grass species. But with this type of modeling, usually a high amount of *in situ* data is usually needed.

More recently, models which have the ability to model the biologically effective irradiance (degree of absorption of radiation in biological molecules) as a function of depth in natural waters (i.e. bio-optical models) have been derived in [11, 4, 12 ] without the need for *in situ* data. In these models, which are based on Lee's model [11, 13], the remote sensing apparent reflectance $R_{rs}$ (ratio of radiance leaving the water to irradiance incident on the water) is described as a function of the absorption $a$, backscattering $b_b$, bottom reflectance $\rho$, and bottom depth $H$ coefficients. Different from models based on empirical regression, Lee's model only assumes the spectral shape of the bottom albedo to be a 550-nm normalized sand reflectance, allowing the change of the albedo intensity, referred as B. Furthermore, no information is needed in addition to the $R_{rs}$ obtained from the hyperspectral sensor. It basically produces an estimate of the $R_{rs}$, and iteratively minimizes an error function by comparing the measured reflectance with the estimated one, thus finally retrieving optimized parameters representing the water column and bottom contributions. This procedure is also known as inversion of optical properties.

Different modifications have been done to Lee's model for different site areas and specific needs. For example, A. Albert and C.D. Mobley [13] used a slightly modified version to study Lake Constance, Germany and simulations extracted from Hydrolight. Davis and Carder [34] applied a slightly modified version of Lee's algorithm in order to extract parameters from Tampa Bay, Florida, and stated that it is useful even for optically dense waters. Also, several methods for finding the minimization of error or optimization schemes have been used. For instance, a Levenberg-Marquardt optimization algorithm was used in [13] for the retrieval of parameters. Also, it is common to perform a reduction in the number of spectral bands for a better spectral fit. Genetic algorithms have been used in [14] as the optimization scheme, but just for the case of optically deep waters (no bottom reflectance is detected by the sensor). This type of algorithm seeks for a global minimum rather than possible local minimum in the error function, thus producing better fits. Recently, Jiménez [31] presented a technique for mapping coastal waters by using Lee's model to retrieve OP's in combination with a Tikhonov regularization parameter which uses *a priori* information on the spectral signatures of the possible materials below the water column.

Recent work by J.A. Goodman [1, 15] has used a modified version of Lee's algorithm to perform an analysis of Kaneohe Bay, Oahu, Hawaii. It incorporates the use of a constrained linear mixing model with four endmembers: sand, coral, algae and zero-shade (dark bottom). Once the water and bottom properties are estimated using the semi-analytical model, the abundance for each spectral endmember at the water surface is calculated and a benthic classification is performed. A similar approach was also studied in [32] where water constituent retrieval is performed using known depths.

This work presents an inversion method [4] where measured remote sensing reflectance is transferred to subsurface remote sensing reflectance and the optical parameters and bottom albedo are retrieved by inverting the subsurface remote sensing reflectance. Also, an unmixing approach similar to that in [1] is included. Presented below are the details of the models used in this work.

## 2.4 Lee's bio-optical model

The apparent optical property $R_{rs}(\lambda)$ is a function of the absorption $a(\lambda)$, volume scattering $\beta(\lambda)$, the bottom albedo $\rho(\lambda)$, bottom depth $H$, the subsurface zenith angle $\theta_w$, the subsurface viewing angle from nadir $\theta$, the viewing azimuth angle from the solar plane $\varphi$ and the constituents in the water. Define

$$\boldsymbol{R_{rs}} = \begin{bmatrix} R_{rs}(\lambda_1) \\ R_{rs}(\lambda_2) \\ \ldots \\ R_{rs}(\lambda_{m-1}) \\ R_{rs}(\lambda_m) \end{bmatrix}$$

where $\lambda$ specifies the band and $m$ the total number of bands. Omitting the $\lambda$, a relationship between above surface and below surface remote sensing reflectance has been developed in [11] and is given by:

$$R_{rs} \approx \frac{0.5 r_{rs}}{1-1.5 r_{rs}} \tag{2.1}$$

where $\theta_w$ is the solar zenith angle and $r_{rs}$ is the subsurface remote-sensing upwelling radiance to the downwelling irradiance evaluated just below the surface that can be expressed as:

$$r_{rs} = r_{rs}{}^{dp}\left(1-\exp\left\{-\left[1+\frac{D_u^C}{\cos(\theta_w)}\right]kH\right\}\right)+\frac{1}{\pi}B\rho\exp\left\{-\left[1+\frac{D_u^B}{\cos(\theta_w)}\right]kH\right\}, \tag{2.2}$$

where $r_{rs}{}^{dp}$ is the remote-sensing reflectance for optically deep waters defined as:

$$r_{rs}{}^{dp} = (0.084+0.170u)u\ . \tag{2.3}$$

Optical path-elongation factors for scattered photons from the water column $D_u^{\,C}$ and $D_u^{\,B}$ are:

$$D_u^B = 1.05(1+5.5u)^{0.5},\ D_u^C = 1.03(1+2.4u)^{0.5} \tag{2.4}$$

$$u = b_b/(a+b_b), \quad \kappa = a + b_b \tag{2.5}$$

The total absorption coefficient is composed of the sum of the absorption of pure water, the gelbstoff absorption and the phytoplankton absorption, as

$$a = a_w + a_\varphi + a_g \tag{2.6}$$

where,

$$a_g = G\left(\exp\left[0.014(440-\lambda_i)\right]\right) \quad 1 \le i \le m \tag{2.7}$$

and

$$a_\varphi = \left\{\left(a_0 + a_1 \ln\left[P\right]\right)P\right\} \tag{2.8}$$

with $G$=0.06(chl-a)$^{0.65}$, where chl-a is the chlorophyll a concentration. $P = a_\varphi(440)$. G is the gelbstoff absorption coefficient of a fixed $\lambda$ at 440nm. $P$ is the phytoplankton absorption coefficient at 440nm. Parameter $b_b$ represents the total backscattering coefficient, composed of the sum of the backscattering coefficients of pure water $b_{bw}$ and suspended particles, $b_{bp}$. Their sum is denoted by:

$$b_b = b_{bw} + b_{bp} \tag{2.9}$$

$b_{\mathrm{bp}}$ is expressed as:

$$b_{bp} = \mathrm{BP}\left(\frac{400}{\lambda_i}\right)^{\mathrm{Y}} \quad 1 \le i \le m \tag{2.10}$$

where BP is the backscattering coefficient at 400nm and Y is the parameter describing the spectral shape, given by:

$$Y \approx 3.44\left(1 - 3.17\exp\left[-2.01 R_{rs}(440)/R_{rs}(490)\right]\right) \tag{2.11}$$

Finally, the backscattering coefficient of pure water is:

$$b_{bw} = 0.0038\left(\frac{400}{\lambda_i}\right)^{4.3} \quad 1 \le i \le m \tag{2.12}$$

Going back to (Equation 2.2), B is the bottom albedo at 550 nm, and $\rho$ is a representative bottom spectrum normalized to 1 at 550nm which in [4] was sand.

Together, these parameters and equations describe the characteristics and interactions of the optical properties of the water column and bottom. With the information acquired from the bottom parameter estimation, the water column effect may be filtered and essentially removed, thus providing a more accurate classification of the bottom. Please refer to Table 2.1 to see the parameter description and units.

**Table 2.2.** Parameter Description and units

| Parameter | Description | Unit |
|---|---|---|
| $A$ | Absorption coefficient, total | $m^{-1}$ |
| $a_\psi$ | Absorption coefficient of phytoplankton pigments | $m^{-1}$ |
| $a_g$ | Absorption coefficients of gelbstoff and detritus | $m^{-1}$ |
| $a_w$ | Absorption coefficients of pure seawater | $m^{-1}$ |
| $a_0, a_1$ | Empirically derived coefficients | -- |
| $b_b$ | Backscattering coefficient, total | $m^{-1}$ |
| $b_{bp}$ | Backscattering coefficient of suspended particles | $m^{-1}$ |
| $b_{bw}$ | Backscattering coefficient of pure seawater | $m^{-1}$ |
| $B$ | Bottom reflectance at 550 nm | -- |
| $BP$ | Combined coefficient for particle-backscattering, view angle and sea state | $m^{-1}$ |
| $D_u^B$ | Distribution function for scattered photons from the bottom | -- |
| $D_u^C$ | Distribution function for scattered photons from the water | -- |
| $x_{s,c,a}$ | Fractional endmember contributions | -- |
| $G$ | Absorption coefficient for gelbstoff and detritus at 440 nm | $m^{-1}$ |
| $H$ | Water depth | m |
| $K$ | Attenuation coefficient | $m^{-1}$ |
| $X$ | Wavelength | nm |
| $B$ | Bottom reflectance (albedo) | -- |
| $P$ | Phytoplankton absorption coefficient at 440 nm | $m^{-1}$ |
| $r_{rs}$ | Subsurface remote sensing reflectance | $sr^{-1}$ |
| $r_{rs}^{dp}$ | Subsurface remote sensing reflectance for optically deep water | $sr^{-1}$ |
| $R_{rs}$ | Surface remote sensing reflectance | $sr^{-1}$ |
| $\theta_w$ | Subsurface solar zenith angle | rad |
| $U$ | Ratio of backscattering coefficient to the attenuation coefficient | -- |
| $Y$ | Spectral power for particle backscattering coefficient | -- |
| $\boldsymbol{\gamma}$ | A vector containing the parameters to retrieve: [H,B,BP,G,P] | -- |

A proper retrieval of the bottom properties, bathymetry and benthic classification is the main focus in this study. A least squares optimization procedure will be used in linear mixing model coefficients and the OP's.

## 2.5 Linear Mixing Model

A linear mixing model is used to model the spectra of the bottom albedo. The expected result is an estimated value of the abundance of each of the endmembers (e.g. coral, sand, algae). The linear mixing model is given by

$$\boldsymbol{b} = \sum_{i=1}^{n} x_i \boldsymbol{a}_i + \boldsymbol{w} = \boldsymbol{A}\boldsymbol{x} + \boldsymbol{w} \tag{2.13}$$

where $\boldsymbol{b}$ is the combined spectral signature, $\boldsymbol{a}_i$ is the spectral signature of the $i$-th endmember, $x_i$ the corresponding fractional abundance, $\boldsymbol{w}$ is the measurement noise (usually assumed Gaussian with zero mean and $\sigma^2 I$ variance), $\mathbf{A} \in \Re^{mxn}$, m the number of spectral bands and $n$ is the number of endmembers [17]. The abundances need to satisfy the constraints that $x_i \geq 0$ and $\sum x_i = 1$. We also tested $\sum x_i \leq 1$ to allow for a dark endmember.

### 2.5.1 Non-Negative Sum Less or Equal to One (NNSLO)

This algorithm deals with the following problem:

$$\arg\min \|A\boldsymbol{x} - \boldsymbol{b}\| \; \textit{subject to } \boldsymbol{x} \geq 0 \textit{ and } \mathbf{1}^{\mathrm{T}} \boldsymbol{x} \leq 1. \tag{2.14}$$

where $\mathbf{1}$ is a vector of ones of dimension $n$. The NNSLO algorithm allows for a dark pixel as a possible spectral signature, thus satisfying the non negative and sum to less or equal to one constraints. This minimization is transformed into a least distance problem which is solved as a Non Negative Least Square Problem and is described in [30].

### 2.5.2 Non-Negative Sum Less or Equal to One (NNSTO)

This unmixing algorithm deals with the following problem:

$$\arg\min \left\| A\boldsymbol{x} - \boldsymbol{b} \right\| \ \textit{subject to}\ \boldsymbol{x} \geq 0 \ \textit{and}\ \mathbf{1}^T x = 1. \tag{2.15}$$

We solve this problem as described in [30] by transforming it to NNSLO problem. Now, it is important to state that in our approach, ***A*** is dependent on the optical properties of the water column. Therefore, during the determination of the bottom albedo the matrix ***A*** will change with the OP's at each pixel. How these OP's are retrieved using Lee's bio-optical model will be discussed next, followed by Goodman's modifications and additions to the model. This algorithm is preferred over the NNSLO since better results were obtained when making the validation of the algorithms (Chapter 4).

## 2.6 Retrieval of bottom and water column optical properties

### 2.6.1 Lee's Inversion

Equation 2.2 is an approximation that describes the remote sensing reflectance just below the water surface and represented as a sum of contributions from the bottom surface reflectance and the water column. This also may be expressed as a function of the total absorption, the total backscattering, the bottom albedo reflectance and the water depth. Due to the nonlinear nature of (2.2), an adequate nonlinear optimization technique must be used. With this optimization scheme, the model's predicted remote sensing reflectance for a given pixel is matched with the measured remote sensing reflectance after proper atmospheric correction and removal of sunglint. Its goal is to retrieve values that describe the composition of the water and the bottom albedo. For every pixel, these retrieved values would be: H, the water depth; B, the bottom albedo for sand at 550nm; BP, which includes a combination of influences of particle backscattering, viewing angle and sea state; G, the absorption coefficient for gelbstoff and detrious at 440 nm and P, the phytoplankton absorption coefficient at 440 nm.

From Lee's model, we state that:

$$\boldsymbol{R_{rs}} = f(\rho,\gamma) \tag{2.16}$$

where

$$\gamma = [P, B, G, BP, H]^T \tag{2.17}$$

The $\rho$ in (2.16) is a 550-nm normalized sand spectra. Equations 2.16 and 2.17 specify that the remote sensing reflectance is a function of the contributions of the water column and the bottom reflectance. The five unknowns in $\gamma$ can be derived by minimizing the differences between the measured and modeled $\boldsymbol{R_{rs}}$. The error to be minimized is described in [26] and it's given by:

$$\boldsymbol{e_{Lee}} = \arg\min_{\gamma}\left(\frac{\left[\sum_{400}^{675}\left(R_{rs}-\hat{R}_{rs}\right)^2+\sum_{750}^{830}\left(R_{rs}-\hat{R}_{rs}\right)^2\right]}{\sum_{400}^{675}\hat{R}_{rs}^{\ 2}+\sum_{750}^{830}\hat{R}_{rs}^{\ 2}}\right) \tag{2.18}$$

For simplicity, the problem to solve is expressed as:

$$(\hat{\gamma}) = \arg\min_{\gamma}\frac{\frac{1}{2}\left\|\boldsymbol{R_{rs}} - \boldsymbol{\hat{R}_{rs}}(\rho,\gamma)\right\|_2^2}{\left\|\boldsymbol{R_{rs}}\right\|_2^2}. \tag{2.19}$$

Although very good results can be obtained by using Lee's bio-optical model in both clear and high-sediment waters, it assumes that sand spectra is the only material at the bottom. With the 550-nm normalized sand spectra multiplied by parameter B, it only describes how 'bright' the pixel is, stating for example that if the B is estimated high for a given pixel, it is probably a bright pixel characterizing the scene as shallow with sand, whereas a low estimated value for B would signify a deeper water or something else like coral or algae. Furthermore, rather than just estimating water quality conditions and depth, the monitoring of the bottom materials is a very important issue for accurate benthic habitat mapping.

### 2.6.2 Goodman's Spectral Unmixing

Using Lee's approach to obtain OP's and water depths, Goodman [1] took advantage of the spectral separability in the different components of hyperspectral imagery to add a linear mixing model to extract bottom composition. Three endmembers were used in his research: coral, algae and sand. He also added a zero-shade endmember to account for overall pixel brightness.

Spectral unmixing was done at the water surface, which was accomplished by transforming the endmember reflectances to surface remote sensing reflectance and then (i.e. using forward modeling) and then unmixing at the water surface. This procedure will be explained in more detail in the next chapter. To define the estimation error it is important to describe Goodman's approach as a two stage procedure. The first step is to retrieve the vector $\gamma$ by using Lee's approach and a second step is to transform each of the endmember spectras to remote sensing reflectance using Lee's forward model, then unmixing. After that, the $\boldsymbol{R_{rs}}$ is modeled as a linear combination of the endmember $\boldsymbol{R_{rs}}$'s and the respective fractional abundances. The error is expressed as:

$$e_{goodman} = \arg\min_{\gamma}\left(\frac{\left[\sum_{400}^{675}\left(R_{rs}-\hat{R}_{rs}\right)^2+\sum_{720}^{800}\left(R_{rs}-\hat{R}_{rs}\right)^2\right]}{\sum_{400}^{675}\hat{R}_{rs}{}^2+\sum_{720}^{800}\hat{R}_{rs}{}^2}\right) \tag{2.20}$$

with $\boldsymbol{R_{rs}}$ is modeled as

$$\hat{\boldsymbol{R}}_{rs} = \sum_{i=1}^{4} x_i \bar{\boldsymbol{R}}_{rs}(\rho_i,\gamma) \tag{2.21}$$

where $x_i$ is the fractional abundance and $\bar{\boldsymbol{R}}_{rs}(\rho_i,\gamma)$ is the i$^{th}$ endmember reflectance $\rho_i$ transformed to surface apparent reflectance $\boldsymbol{R_{rs}}$. For simplicity, the problem to solve is

$$(\hat{x}) = \arg\min_{x\geq 0, x^T 1=1} \frac{\frac{1}{2}\left\|\boldsymbol{R}_{rs} - \sum_{i=1}^{4} x_i \bar{\boldsymbol{R}}_{rs}(\rho_i,\gamma)\right\|_2^2}{\left\|\boldsymbol{R}_{rs}\right\|_2^2}. \tag{2.22}$$

The objective for modeling remote sensing reflectance at the water surface as used in [1] is to retrieve benthic composition after obtaining the water optical properties, the bottom albedo and the water depth. It is instructive to show Lee's and Goodman's approaches in an algorithmic point of view in order to make a starting point for the development of an improved method.

## 2.7 Lee's Inversion Model with Goodman's Unmixing (LIGU)

The full procedure required to obtain water properties, depth and benthic composition is described here. This is based on the Lee's inversion model. It was programmed in order to test if the results obtained for a given data set are similar to those obtained by Goodman's algorithm. Specifically, this was done to test whether the same results could be obtained in MATLAB as previously obtained by Goodman using IDL. It does not have any changes made for improving results. It is just a mirror to what has been done already. Basically, a set of initial parameters (i.e. H, B, BP, G, P) is entered in the optimization routine, which has an error function that minimizes the sum of squares of the error vector $\boldsymbol{e_{lee}}$ (recall Equation 2.18). After a set of values of OP's is retrieved using the nonlinear optimization routine, abundances are estimated to provide a latter classification of the coastal scene.

A 550-nm normalized sand reflectance, multiplied by parameter B is the only reflectance used for approximating the bottom reflectance for a given pixel in the inversion model. The abundance estimation is done by using the retrieved vector of optimized values, and constructing a remote sensing reflectance endmember matrix $A$. A vector of abundances will be obtained by linearly unmixing the pixel of interest $\boldsymbol{R_{rs}}$ with $A$. Figure 2.4 shows Lee's inversion model. The vector of optical properties, bottom albedo B and water depths are entered as input to Lee's model, and this returns an estimated remote sensing reflectance vector. Then the error (Equation 2.18) is calculated for the $i^{th}$ iteration.

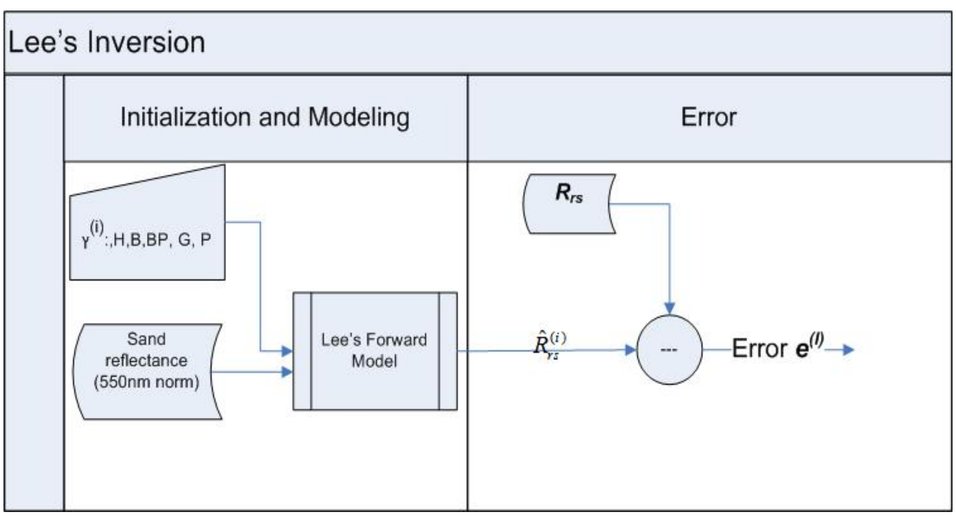


**Figure 2.3.** Lee's Inversion Algorithm.

Once the squared error is minimized, a solution vector of water properties is obtained. This solution vector is then used for estimating the abundances. Refer to Figure 2.5, a representation of how the abundance estimates are retrieved. This is an additional processing step added by Goodman to Lee's inversion algorithm. For the i$^{th}$ iteration, the retrieved vector of OP's and water depth from Lee' model is used for transforming the endmember spectras to remote sensing reflectance, thus creating the endmember matrix $\boldsymbol{A}$, then used to retrieve the abundance vector $\hat{\boldsymbol{x}}$.

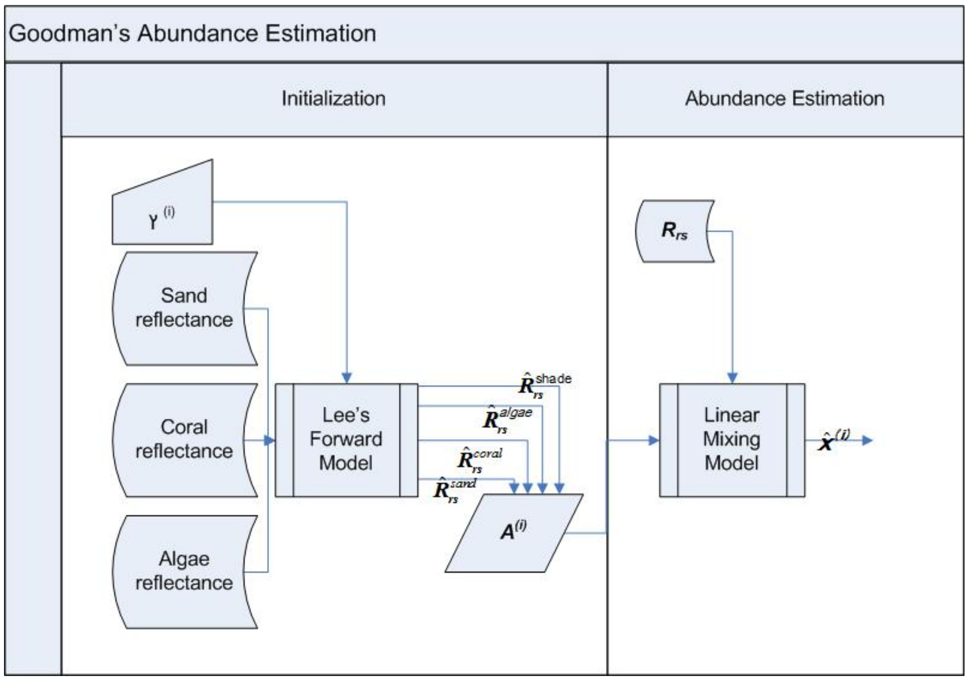


**Figure 2.4.** Goodman's Unmixing Procedure.

The pseudo code for Lee's Inversion model with Goodman's Unmixing (LIGU) is given by:

Initialize $\gamma$ and compute $Y$ as in (2.11).

While $\boldsymbol{e_{lee}}$ > Tolerance

- Input $\gamma$ and B into Lee's Forward Model.
- Compute $\hat{\boldsymbol{R}}_{rs} = f(\gamma, \rho_i)$.
- Minimize (2.19).

Iterate until Convergence

- Compute the endmember matrix:

$$\boldsymbol{A} = \left[ \overline{\boldsymbol{R}}_{rs}^{sand}(\rho_i, \gamma) \quad \overline{\boldsymbol{R}}_{rs}^{coral}(\rho_i, \gamma) \quad \overline{\boldsymbol{R}}_{rs}^{algae}(\rho_i, \gamma) \right].$$

- Estimate fractional abundance vector $\hat{\boldsymbol{x}}$ = unmix ($\boldsymbol{A}$, $\boldsymbol{R_{rs}}$) by minimizing (2.22).
- Model remote sensing reflectance as $\hat{\boldsymbol{R}}_{rs} = \boldsymbol{A}\,\hat{\boldsymbol{x}}$ .
- Compute Goodman's error (2.20).

## 2.8 Conclusions

In this Chapter, the problem of retrieving optical properties of the water column and the bottom reflectance approximation was introduced. Different approaches to solve this problem were described, more specifically Lee's bio-optical model and Goodman's Linear Mixing Model. This process was summarized as the Lee's Inversion Model and Goodman's Unmixing (LIGU) algorithm. This discussion facilitates the introduction of a new approach combining these two techniques.

# Chapter 3

# Inversion Algorithm

## 3.1 Introduction

This Chapter presents the inversion algorithm developed in this research.

## 3.2 Modeling Remote Sensing Reflectance

As a simplifying assumption, the modeling of remote sensing reflectance for a given pixel in a coastal scene is assumed to be expressed as a linear combination of endmembers. In order to do that, both the water and bottom properties as well as the fractional abundances vector must be properly estimated. The main goal is to find a vector $\gamma$ and a vector $\boldsymbol{x}$ such that minimizes an error $\boldsymbol{e}$. Modifications in the way these OP's and the abundances are calculated, clearly affect the modeling of the $\boldsymbol{R_{rs}}$ thus giving different errors. There is an interest for making this error as small as possible. For that reason, several changes were made to the error function used by the nonlinear optimization scheme, where the sum of squares of this error is minimized. This error function accepts a vector $\gamma$ and returns a vector $\boldsymbol{e}$, which are the objective functions evaluated at $\gamma$. When these evaluations make the sum of squares error to reach a specified tolerance, or no significant change after iteration is obtained, the algorithm stops.

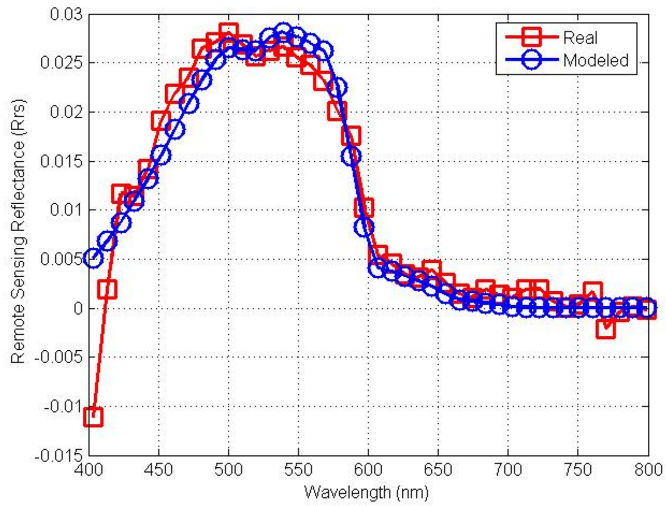


**Figure 3.1.** Curve fitting of remote sensing reflectance.

The estimation of remote sensing reflectance $\hat{\boldsymbol{R}}_{rs}$ may be analyzed using either unmixing at the top of the water surface or at the bottom. The approaches discussed here are catalogued using that as criteria. One is a method that performs unmixing at the bottom level of the ocean, and the other is a method that performs unmixing at the top level of the ocean surface.

It is important to mention that a set of initial values for $\gamma$ is necessary in each of the approaches in order to obtain an optimized estimate. Initial values for abundances are not required.

For simplicity of reading, a review of the most important Lee's semi-analytical model equations is shown in the Table 3.1.

**Table 3.1.** Semi-analytical model equations.

| Equation | |
|---|---|
| $a = a_w + \left[a_0 + a_1 \ln(P)\right]P + Gexp\left[-0.015\left(\lambda - 440\right)\right]$ | (3.1) |
| $Y \approx 3.44\left(1 - 3.17\exp\left[-2.01R_{rs}(440)/R_{rs}(490)\right]\right)$ | (3.2) |
| $b_b = 0.0038\left(400/\lambda\right)^Y + BP(400/\lambda)^{4.3}$ | (3.3) |
| $u = b_b \big/ \left(a + b_b\right)$ | (3.4) |
| $r_{rs}{}^{dp} = (0.084 + 0.170u)u$ | (3.5) |
| $D_u^B = 1.05(1+5.5u)^{0.5}$ | (3.6) |
| $D_u^C = 1.03(1+2.4u)^{0.5}$ | (3.7) |
| $\kappa = a + b_b$ | (3.8) |
| $r_{rs} = r_{rs}{}^{dp}\left(1 - \exp\left\{-\left[1 + \frac{D_u^C}{\cos(\theta_w)}\right]kH\right\}\right) + \frac{1}{\pi}B\rho\exp\left\{-\left[1 + \frac{D_u^B}{\cos(\theta_w)}\right]kH\right\}$ | (3.9) |
| $R_{rs} \approx \frac{0.5r_{rs}}{1 - 1.5r_{rs}}$ | (3.10) |

## 3.3 A Simple Two-Step Retrieval Algorithm

After knowing how the error function is designed in order to retrieve both the OP's and the benthic mapping, there are additional ways to address this problem in a more efficient way. It is intended to do the minimization of error by combining iteratively both the inversion of water properties as well as the abundance estimates. At first glance, the simplest way to do this is by a two-stage algorithm in which a Lee's inversion extract the OP's and bathymetry, and second stage which uses the first estimation of the ***R<sub>rs</sub>*** and continue to get a smaller error by introducing coral and algae spectras as an alternative to the sand spectra. Unlike Goodman's approach, the nonlinear optimization routine will estimate OP, bathymetry and abundances together. This approach does not limit the bottom reflectance to be sand, but by adding a linear mixture model, the bottom reflectance can be constructed by a linear combination of sand, coral and algae.

Define $\hat{\boldsymbol{R}}_{rs}$ as the estimated vector of the remote sensing reflectance at the water surface from the bio-optical model at wavelength $\lambda$. So, we will use the following error:

$$\boldsymbol{e} = \begin{bmatrix} e(\lambda_1) \\ e(\lambda_2) \\ \vdots \\ e(\lambda_{m-1}) \\ e(\lambda_m) \end{bmatrix} = \boldsymbol{R}_{rs} - \hat{\boldsymbol{R}}_{rs} = \begin{bmatrix} R_{rs}(\lambda_1) - \hat{R}_{rs}(\lambda_1) \\ \vdots \\ R_{rs}(\lambda_m) - \hat{R}_{rs}(\lambda_m) \end{bmatrix}, \tag{3.11}$$

where

$$e(\lambda_i) = \hat{R}_{rs}(\lambda_i) - \hat{\boldsymbol{R}}_{\boldsymbol{rs}}(\lambda_i) \tag{3.12}$$

We must find a $\gamma$ and a $x$ such that minimizes the following:

$$(\hat{x}, \hat{\gamma}) = \underset{\gamma, x}{\arg\min} \frac{\frac{1}{2}\left\| \boldsymbol{R}_{\boldsymbol{rs}} - \sum_{i=1}^{3} x_i \bar{R}(\rho_i, \gamma) \right\|_2^2}{\left\| \boldsymbol{R}_{\boldsymbol{rs}} \right\|_2^2}. \tag{3.13}$$

Note that the division by the norm of $\boldsymbol{R}_{\boldsymbol{rs}}$ is to make this criterion independent of the empirical data size [16]. It is important to mention that this problem is bound constrained, which means that the optimization routine must keep the values of the estimate between a range of values. The reason for this is that certain values are not physically possible (like a negative value) or the model is expecting a specific range of values, like, for example, the water depth. These constraints keep the estimates within reasonable physically acceptable limits.

This process can be subdivided in two stages. The first stage is to retrieve estimates of the OP's and water depths using Lee's algorithm. Now that the initialization is completed, both the estimated vector $\gamma$ and $\rho$ will be used in a second stage, where the linear mixing model will be used to model the remote sensing reflectance. Figure 3.4 shows a graphical representation of the approach. Next we will show implementations of this approach where unmixing occurs at the bottom and at the surface.

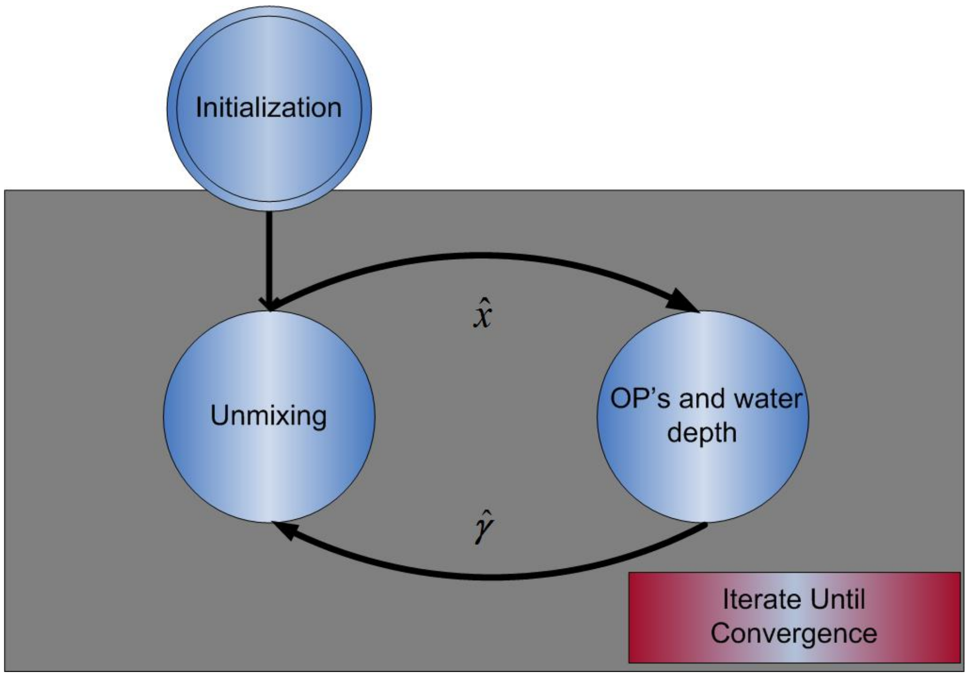


**Figure 3.4.** Two-stage retrieval algorithm.

The simple two step algorithm is described below:

Initialize $\gamma$ and compute Y as in (3.2)

While $\boldsymbol{e_{lee}}$ > Tolerance of 1$^{st}$ Stage.

- Input $\gamma$ and B into Lee's Forward Model.
- Compute $\hat{\boldsymbol{R}}_{rs} = f(\gamma, \rho_i)$.
- Minimize (2.19).

Iterate until Convergence

While $\boldsymbol{e_{lee}}$ > Tolerance of 2$^{nd}$ Stage.

- Compute endmember matrix:

$$\boldsymbol{A} = \left[ \overline{\boldsymbol{R}}_{rs}(\gamma, \rho_{sand}) \quad \overline{\boldsymbol{R}}_{rs}(\gamma, \rho_{coral}) \quad \overline{\boldsymbol{R}}_{rs}(\gamma, \rho_{algae}) \quad \right]$$

- Estimate fractional abundance vector $\hat{\boldsymbol{x}}$ = unmix ($\boldsymbol{A}$, $\boldsymbol{R_{rs}}$) solving (2.22).
- Model remote sensing reflectance as $\hat{\boldsymbol{R}}_{rs} = \boldsymbol{A}\,\hat{\boldsymbol{x}}$ .
- Compute the error as in (2.20).

Iterate until convergence.

## 3.4 Unmixing at the water surface or at the bottom?

There are two different ways to do the linear unmixing: at the water surface or at the bottom. A linear mixing model used at top of the water surface would be similar to what was done in [1], where different materials reflectance spectral signatures (e.g. sand, coral and algae) were transformed using Lee's semi-analytical model to surface reflectance. Another way of thinking it is to perform the estimation of water optical properties to characterize the water column, and perform the spectral separation at the bottom. Our interest is to test which approach will result in a better estimate of bottom properties.

### 3.4.1 Combined Inversion with Linear Unmixing at the Water Surface (CIUS)

We define the light interaction in the water column to be nonlinear (Equation 3.9). Additionally, in a similar approach to that used by Goodman, a simplifying assumption [15] is used for the mixing process. We assume that the remote sensing reflectance at the water surface is a linear mixture of the remote sensing reflectance contributions by the individual bottom types. It is also assumed that the contribution of each element in the bottom is only affected by the water column with no interaction with the other bottom types inside the pixel. Therefore, the modeled remote sensing reflectance at the water surface is given by:

$$\hat{\boldsymbol{R}}_{rs} = \sum_{\boldsymbol{i}=1}^{3} \boldsymbol{x}_i \overline{R}_{rs}(\rho_{\boldsymbol{i}}, \gamma) \tag{3.14}$$

where $i$ is the index for the endmembers. In matrix form, this model can be expressed as:

$$\hat{\boldsymbol{R}}_{rs} = \boldsymbol{A}\boldsymbol{x}, \tag{3.15}$$

where

$$\boldsymbol{A} = \left[ \overline{\boldsymbol{R}}_{rs}^{sand}(\rho_{\boldsymbol{i}}, \gamma) \quad \overline{\boldsymbol{R}}_{rs}^{coral}(\rho_{\boldsymbol{i}}, \gamma) \quad \overline{\boldsymbol{R}}_{rs}^{algae}(\rho_{\boldsymbol{i}}, \gamma) \right], \tag{3.16}$$

Each column represents transformed endmember spectra for sand, coral and algae converted into remote sensing reflectance space. The matrix $\boldsymbol{A}$ and the measured $\boldsymbol{R}_{rs}$ are entered as input to the unmixing algorithm, which returns the abundances vector $\boldsymbol{x}$. Then the matrix $\boldsymbol{A}$ multiplied by $\boldsymbol{x}$ will be the new estimated remote sensing reflectance. Finally, the problem to solve is:

$$(\hat{x}, \hat{\gamma}) = \arg\min_{\gamma, x} \frac{\frac{1}{2}\left\| \boldsymbol{R}_{rs} - \sum_{i=1}^{3} x_i \overline{R}(\rho_i, \gamma) \right\|_2^2}{\left\| \boldsymbol{R}_{rs} \right\|_2^2}. \tag{3.17}$$

The abundance estimate is obtained through adjusting each of the endmembers spectras to compensate for water column effects. The unmixing algorithm is also constrained to be nonnegative and that the sum of the fractional abundances equals one. Using this type of approach of the $\boldsymbol{R}_{rs}$, the estimation of water properties and the abundances may be implemented simultaneously. Figure 3.5 shows this process for the i$^{th}$ iteration.

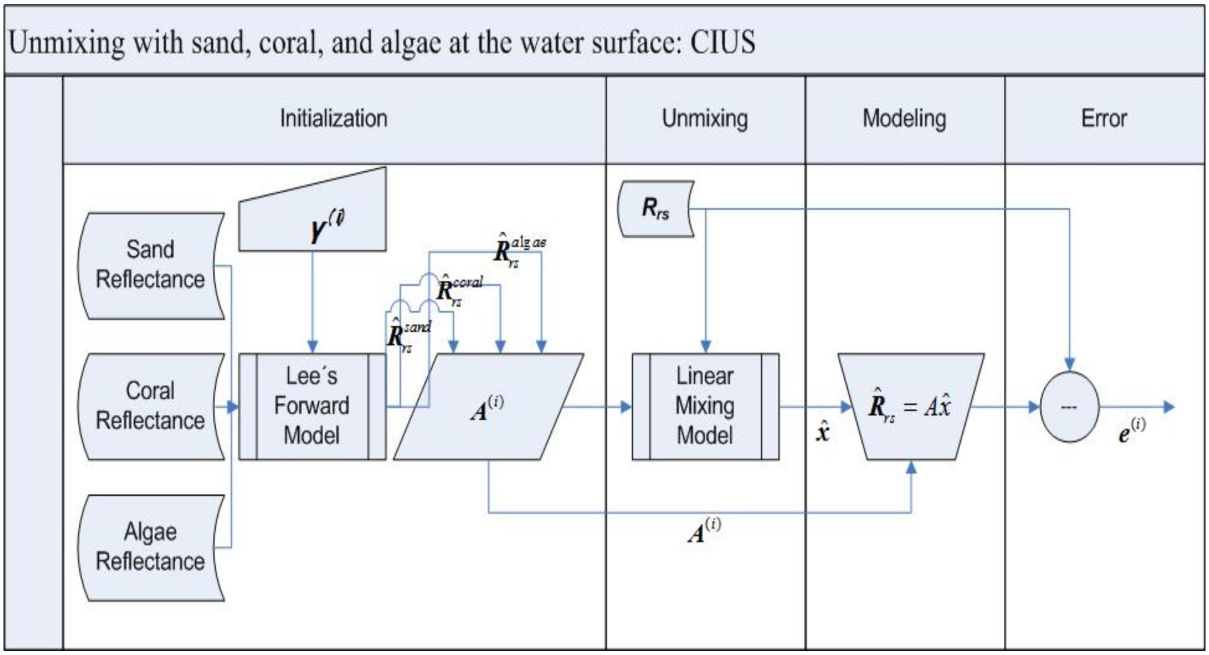


**Figure 3.5.** CIUS representation.

This type of inversion algorithm was tested with both real and simulated data. It works properly for synthetic data but seems to fail or provide poor results when dealing with real data. For that reason, the development of an approach that performs spectral unmixing at the bottom was performed. Other ways of implementation like using 550-nm normalized reflectances and the parameter B estimation were tried without success, even though performed faster. A pseudo code for the CIUS algorithm is now presented as:

Initialize $\gamma$ and compute $Y$ *(no B needed)*.

While $\boldsymbol{e}$ > Tolerance

- Compute matrix $\boldsymbol{A}$.
- Estimate fractional abundance vector $\boldsymbol{x}$ = unmix ($\boldsymbol{A}$, $\boldsymbol{R_{rs}}$) solving (2.22).
- Model remote sensing reflectance as $\hat{\boldsymbol{R}}_{rs} = \boldsymbol{A}\hat{\boldsymbol{x}}$.
- Solve (3.17).

Iterate until convergence.

### 3.4.2 Combined Inversion with Linear Unmixing at the Bottom of the Ocean (CIUB)

Observing that the subsurface remote sensing reflectance $\boldsymbol{r_{rs}}$ is expressed as the sum of the contributions from the water column and the bottom (3.9), one can take advantage of using $\boldsymbol{r_{rs}}$ instead of $\boldsymbol{R_{rs}}$. Instead of trying to approximate above the surface measured remote sensing reflectance $\boldsymbol{R_{rs}}$, we try to fit the subsurface remote sensing reflectance, namely $\boldsymbol{r_{rs}}$. In order to do so, the error calculation criteria is to modify (3.11) to:

$$\boldsymbol{e} = \begin{bmatrix} e(\lambda_1) \\ e(\lambda_2) \\ \vdots \\ e(\lambda_{m-1}) \\ e(\lambda_m) \end{bmatrix} = \boldsymbol{r}_{rs} - \hat{\boldsymbol{r}}_{rs} = \begin{bmatrix} r_{rs}(\lambda_1) - \hat{r}_{rs}(\lambda_1) \\ \vdots \\ r_{rs}(\lambda_m) - \hat{r}_{rs}(\lambda_m) \end{bmatrix}, \tag{3.18}$$

and (3.12) as

$$e_{r_{rs}}(\lambda_i) = r_{rs}(\lambda_i) - \hat{r}_{\boldsymbol{rs}}(\lambda_i) \tag{3.19}$$

To retrieve the abundance vector and optical parameters, we solve the optimization problem:

$$(\hat{x}, \gamma) = \underset{x \geq 0, x^T 1 = 1, \gamma}{\arg\min} \frac{\frac{1}{2} \left\| \boldsymbol{r_{rs}} - \hat{\boldsymbol{r}}_{\boldsymbol{rs}}(\gamma, \rho) \right\|_2^2}{\left\| \boldsymbol{r_{rs}} \right\|_2^2}. \tag{3.20}$$

were $\boldsymbol{e}$ is given in (3.18).

The vector $\boldsymbol{\rho}=A\boldsymbol{x}$ represent the bottom albedo spectra as a linear mixing of the spectra of the endmembers. We now illustrate the steps to perform the minimization of error in (3.20).

From (3.10), it is straight-forward to convert measured apparent reflectance to subsurface apparent reflectance as:

$$r_{rs} = \frac{R_{rs}}{0.5 + 1.5R_{rs}} \tag{3.21}$$

From Lee's model, and letting the bottom reflectance be modeled as $\boldsymbol{\rho}=A\boldsymbol{x}$, equation (3.9) is modified for estimation purposes as follows:

$$\hat{r}_{rs} = r_{rs}{}^{dp}\left(1 - \exp\left\{-\left[1 + \frac{D_u^C}{\cos(\theta_w)}\right]kH\right\}\right) + \frac{1}{\pi}B\rho\exp\left\{-\left[1\frac{D_u^B}{\cos(\theta_w)}\right]kH\right\} \tag{3.22}$$

The combined ρ is normalized to be equal to 1 at to 550 nm and multiplied by the bottom scaling parameter B. The reason behind this is to add one more degree of freedom in the search for a method that produces the best results possible. With the normalization at 550 nm and the addition of the scaling parameter B, we combine Lee's inversion model that normalizes a sand reflectance to 550 nm and uses the parameter B to scale the bottom albedo in combination with the unmixing concept of Goodman.

The right hand side (RHS) of (3.22) comes from the previously described model with the estimated OP's. The LHS is the measured subsurface remote sensing reflectance. Making this iterative, and subtracting the water column contributions from the RHS term, we obtain

$$r_{rs} - r_{rs}{}^{dp}\left(1 - \exp\left\{-\left[\frac{1}{\cos(\theta_w)} + D_u^C\right]kH\right\}\right) = \frac{a_i^T\hat{x}}{\pi}\exp\left\{-\left[\frac{1}{\cos(\theta_w)} + D_u^B\right]kH\right\} \tag{3.23}$$

where $a_i^T$ is the i[th] row of $\boldsymbol{A}$.

Let the LHS of equation (3.23) be our vector $\boldsymbol{b}$, and let a new matrix $\boldsymbol{A}$ be composed as:

$$\hat{a}_i = \frac{a_i}{\pi}\exp\left\{-\left[\frac{1}{\cos(\theta_w)} + D_u^B\right]kH\right\} \tag{3.24}$$

Finally, a linear mixing model can be applied to estimate the proper abundances as

$$\hat{\boldsymbol{x}}^{(i)} = unmix(\boldsymbol{A}, \boldsymbol{b}^{(i)}) \tag{3.25}$$

Figure 3.6 shows a flowchart of this method. In the modeling stage, note that OP's, bathymetry, and abundance estimates are calculated inside the forward model.

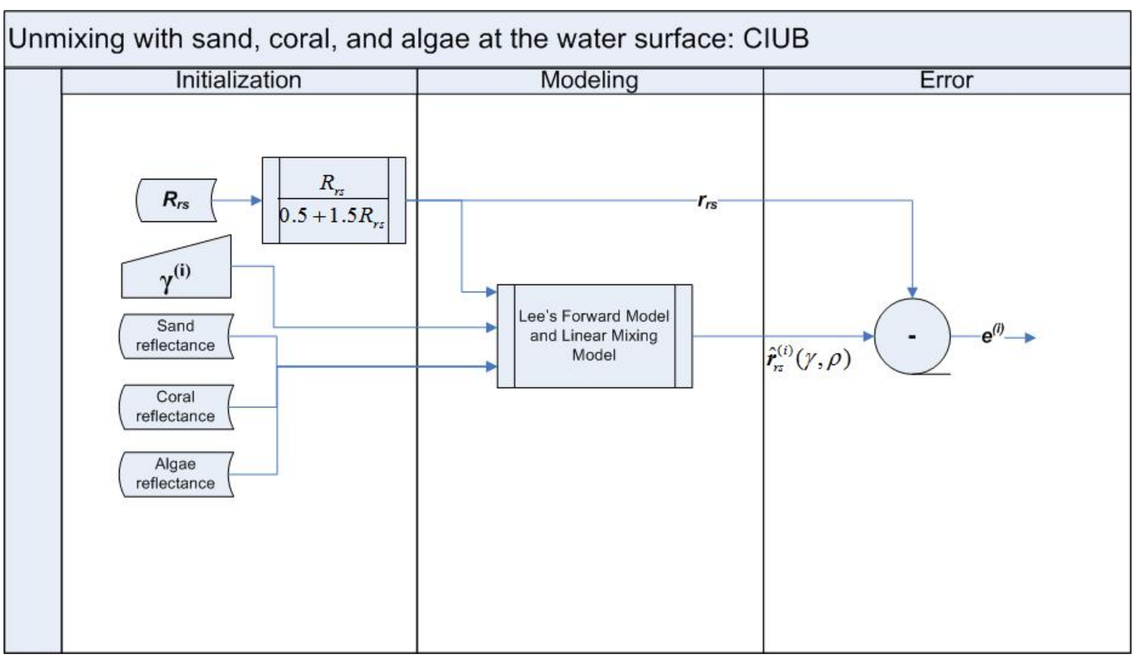


**Figure 3.6.** CIUB representation.

This approach has its advantages over the previously discussed methods. It does not make the assumption that the remote sensing reflectance at the water surface is a linear mixture of the remote sensing reflectance contributions by the individual bottom types, since it works directly with the subsurface apparent reflectance. It is treating the abundance problem as partially linear, and accounting for the nonlinear nature of the optical properties that describe the water column. Thus, it is a more realistic approach, and mathematically simpler.

Furthermore, the pseudo code for the CIUB is presented as:

Initialize $\gamma$ and compute $Y$.

Convert $\boldsymbol{R_{rs}}$ to $\boldsymbol{r_{rs}}$.

While $\boldsymbol{e}_{\boldsymbol{rrs}}$ > Tolerance

- Compute matrix $\boldsymbol{A}$ as in (3.24).
- Compute $\boldsymbol{b} = \hat{r}_{rs}^{(0)} - r_{rs}^{\;dp}\left(1 - \exp\left\{-\left[\frac{1}{\cos(\theta_w)} + D_u^C\right]kH\right\}\right)$.
- Estimate fractional abundance vector $\boldsymbol{x}$ = unmix ($\boldsymbol{A}$, $\boldsymbol{b}$).
- Normalize $\boldsymbol{Ax}$ at 550 nm and multiply by B.
- Model subsurface remote sensing reflectance as in (3.22).
- Solve (3.20).

Iterate until convergence.

## 3.5 Conclusions

An existing method for retrieving OP's, bathymetry and benthic compositions was explained. It used the commonly used Lee's inversion scheme and an added a linear mixing model to attack the problem of benthic classification. Furthermore, two new approaches were described as possible improvements to the already existing systems: the CIUS and the CIUB. The difference of the newer ones is the location where the mixing is performed: at the water surface in a fashion similar to Goodman's, or at the bottom.

# Chapter 4

# Algorithm Validation

## 4.1 Introduction

In this chapter, both real and simulated data is used to test, compare and validate the new algorithms presented in Chapter 3. Synthetic data was generated in order to assure that the algorithms work mathematically correct and to study and compare their performance on shallow and deep waters, as well as clear and optically dense waters. The hyperspectral data used for the validation of the algorithm is a portion of pixels taken from a hyperspectral image of Kaneohe Bay, Hawaii taken using the AVIRIS sensor. Depth measurements taken by the Scanning Hydrographic Operational Airborne Lidar Survey (SHOALS) will be compared with the depth estimates of the model. Included here is basic information regarding the preprocessing of the hyperspectral images, including the atmospheric and the sunglint corrections, the basic characteristics of SHOALS and a description of the endmembers selected for the unmixing.

All tests and code implementation were done using MATLAB. The function *lsqnonlin* from Matlab's Optimization Toolbox was used to compute a solution of the OP's parameters vector $\gamma$. It uses a Conjugate Gradient algorithm to minimize the sum of squares error. A routine was also implemented to calculate the modeled subsurface surface remote sensing reflectance vector as specified by (2.2). Previous work based on sensitivity analysis of these parameters [1] provided the ability to identify a range of viable values, thus providing upper and lower bounds, given in Table 4.1.

A tolerance of $10^{-10}$, or maximum number of iterations of 1000 were selected as the stopping criteria for the nonlinear optimization routine. The simulations were run in a Pentium 4 processor clocked at 3.06 GHz and 1GB of RAM using Windows XP OS.

**Table 4.1.** Range of values for optimization

| | Lower Value | Upper Value |
|---|---|---|
| H | 0.2 | 33 |
| BP | 0.001 | 0.5 |
| G | 0.002 | 3.5 |
| P | 0.05 | 1 |

## 4.2 Simulated Data

This section will be subdivided into two different parts, accounting for clear waters and for optically dense waters. On each experiment, water depths of 1, 5, 10, 20, 30 and 50 meters were tested to observe the limitations on the abundance estimation and optical properties as depth increases. The following set of values was used in order to create the pixels:

**Table 4.2.** Parameter values for pixel creation.

| Parameter | H | BP | G | P |
|---|---|---|---|---|
| Clear | 1,5,10,15,20,30,50 | 0.01 | 0.05 | 0.05 |
| Optically Dense | 1,5,10,15,20,30,50 | 0.20 | 1.00 | 0.50 |

Because the approach of doing unmixing at the bottom surface makes an estimate of B, let it be a constant value, B= 0.4. Initial values were set to be 40% different than the real values. The synthetic mixed pixel was set to have 50% sand, 30% coral and 20% algae. The retrieved values obtained from the optimization routine on each set of parameters are presented below. The error statistic $R^2$ is also presented. It measures the proportion of the variability of the observations around the mean. The closer the $R^2$ value to one, the better fit.

### 4.2.1 Experiment 1: Simulating Clear Waters

Noise free synthetic pixels simulating clear water in terms of low phytoplankton and absorption were run through the inversion algorithm. Table 4.3 show results for the approach using the linear mixing model at the bottom surface (CIUB). Table 4.4 describes results obtained with the approach that uses the linear mixing model at top of the water surface (CIUS).

**Table 4.3.** Optimization results for synthetic clear water pixels with CIUB

| Depth (m) | H | BP 0.01 | G 0.05 | P 0.05 | Sand 0.5 | Coral 0.2 | Algae 0.3 | $R^2$ |
|---|---|---|---|---|---|---|---|---|
| 1 | 1.0000 | 0.0100 | 0.0500 | 0.0500 | 0.5000 | 0.2000 | 0.3000 | 1 |
| 5 | 5.0000 | 0.0100 | 0.0500 | 0.0500 | 0.5000 | 0.2000 | 0.3000 | 1 |
| 8 | 7.9999 | 0.0100 | 0.0500 | 0.0500 | 0.5000 | 0.2000 | 0.3000 | 1 |
| 10 | 9.9998 | 0.0100 | 0.0500 | 0.0500 | 0.5000 | 0.1999 | 0.3001 | 1 |
| 15 | 14.9994 | 0.0100 | 0.0500 | 0.0500 | 0.4999 | 0.1999 | 0.3001 | 1 |
| 20 | 19.8934 | 0.0100 | 0.0500 | 0.0499 | 0.4876 | 0.1783 | 0.3342 | 1 |
| 30 | 18.6783 | 0.0098 | 0.0502 | 0.0478 | 0 | 0.1618 | 0.8382 | 1 |
| 50 | 23.5210 | 0.0099 | 0.0499 | 0.0492 | 0 | 0.8508 | 0.1492 | 1 |

**Table 4.4.** Optimization results for synthetic clear water pixels with CIUS.

| Water depth (m) | BP 0.01 | G 0.05 | P 0.05 | Sand 0.5 | Coral 0.2 | Algae 0.3 | BP 0.01 | $R^2$ |
|---|---|---|---|---|---|---|---|---|
| 1 | 0.9691 | 0.0043 | 0.0435 | 0.0389 | 0.4480 | 0.1512 | 0.4008 | 1 |
| 5 | 4.9439 | 0.0099 | 0.0495 | 0.0493 | 0.4748 | 0.2229 | 0.3023 | 1 |
| 8 | 7.9524 | 0.0100 | 0.0499 | 0.0497 | 0.4844 | 0.2150 | 0.3006 | 1 |
| 10 | 9.9595 | 0.0100 | 0.0500 | 0.0498 | 0.4885 | 0.2100 | 0.3015 | 1 |
| 15 | 14.9587 | 0.0100 | 0.0500 | 0.0500 | 0.4936 | 0.2046 | 0.3017 | 1 |
| 20 | 19.2653 | 0.0100 | 0.0501 | 0.0497 | 0.4157 | 0.0572 | 0.5270 | 1 |
| 30 | 18.8048 | 0.0098 | 0.0501 | 0.0478 | 0 | 0.1182 | 0.8818 | 1 |
| 50 | 29.2572 | 0.0100 | 0.0501 | 0.0497 | 0 | 1.0000 | 0.0000 | 1 |

Although almost perfect fittings to the $r_{rs}$ and the $R_{rs}$ curves were attained in terms of the $R^2$ statistic, results show that the both the abundance estimations and the OP's retrieval are affected as water depth increases. The abundance estimates were poor for water depths above 20 meters, where coral and algae fractions were under estimated even though the OP's were not critically affected (i.e., the OP's can be effectively obtained at deeper depths than the bottom contributions). It is also notable an underestimation of water depth H for simulated depths of 20 meters or more. Good estimates of BP, G and P for all depths have been obtained. This makes sense since these parameters mostly describe optical properties of the water column, not the bottom. Even when there is zero contribution coming from the bottom, these OP's seem to be well retrieved. As observed, using the CIUB seems to estimate slightly better than the CIUS. Both underestimate the values of H for water depth greater than those 20 meters.

### 4.2.2 Experiment 2: Simulating Optically Dense Waters

The idea of this experiment is to test how accurate the model is when dealing with optically dense waters. As with the past experiment, both of the new algorithms will be tested using synthethic pixels for increasing water depths synthetic pixels.

**Table 4.5.** Optimization results for synthetic optically dense water pixels with CIUB

| Water depth (m) | H | BP | G | P | Sand | Coral | Algae | $R^2$ |
|---|---|---|---|---|---|---|---|---|
| | | 0.2 | 1 | 0.5 | 0.5 | 0.2 | 0.3 | |
| 1 | 1.0000 | 0.2000 | 1.0000 | 0.5000 | 0.5000 | 0.2002 | 0.2998 | 1 |
| 5 | 4.8006 | 0.2000 | 1.0000 | 0.5000 | 0.5843 | 0.4126 | 0.0030 | 1 |
| 8 | 5.0235 | 0.2000 | 0.9999 | 0.5000 | 1.0000 | 0.0000 | 0.0000 | 1 |
| 10 | 6.0564 | 0.2000 | 0.9999 | 0.5000 | 1.0000 | 0.0000 | 0.0000 | 1 |
| 15 | 9.0583 | 0.2000 | 0.9999 | 0.5000 | 1.0000 | 0.0000 | 0.0000 | 1 |
| 20 | 12.0583 | 0.2000 | 0.9999 | 0.5000 | 1.0000 | 0.0000 | 0.0000 | 1 |
| 30 | 18.0583 | 0.2000 | 0.9999 | 0.5000 | 1.0000 | 0.0000 | 0.0000 | 1 |
| 50 | 30.0583 | 0.2000 | 0.9999 | 0.5000 | 1.0000 | 0.0000 | 0.0000 | 1 |

Observe that the estimates are significantly affected with the increase of water optically denseity. In contrast with clear waters, it starts to underestimate water depth before getting to 10 meters. Also the fractional abundances are also notably affected after the 5 m depth, probably causing to misclassify the bottom at depths of the three to four meters. The parameters BP, P and G seem to be the best estimated values overall, stating again that they are parameters that exclusively describe the water column.

Now taking a look to Table 4.6, very poor abundance estimates are obtained as well as OP's and water depths. Just as shallow as 5 meters depth, the estimates are poor. For water depth greater than 20 meters, the abundance algorithm diverges. We are still getting good estimates of BP, G and P, but not as good as the unmixing at the bottom algorithm.

**Table 4.6.** Optimization results for synthetic optically dense water pixels with CIUS

| Water depth (m) | H | BP 0.2 | G 1 | P 0.5 | Sand 0.5 | Coral 0.2 | Algae 0.3 | $R^2$ |
|---|---|---|---|---|---|---|---|---|
| 1 | 1.0000 | 0.1999 | 1.0029 | 0.4949 | 0.4853 | 0.2211 | 0.2935 | 1 |
| 5 | 3.9363 | 0.1998 | 1.0002 | 0.4990 | 0.6476 | 0.3524 | 0.0000 | 1 |
| 8 | 4.8449 | 0.1998 | 1.0014 | 0.4984 | 0.9531 | 0.0469 | 0.0000 | 1 |
| 10 | 5.5968 | 0.1998 | 1.0010 | 0.4983 | 1.0000 | 0.0000 | 0.0000 | 1 |
| 15 | 7.5144 | 0.1998 | 1.0009 | 0.4983 | 0.0000 | 0.0000 | 1.0000 | 1 |
| 20 | 11.1603 | 0.2000 | 1.0002 | 0.4998 | --- | --- | --- | 1 |
| 30 | 17.7016 | 0.1598 | 0.7843 | 0.3562 | --- | --- | --- | 1 |
| 50 | 30.0000 | 0.1200 | 0.6000 | 0.3000 | --- | --- | ---- | 0.9609 |

Notice that performing the CIUB is slightly better than the CIUS for both clear water and optically dense water pixels. This analysis deals with created pixels, and dealing with this kind of data is usually better than when dealing with real data. Let now see what happens with AVIRIS pixels.

## 4.3 Real Data

The hyperspectral data used for the validation of the algorithm was first atmospheric and sunglint corrected. Also, the number of bands from the AVIRIS image was subset from its original 224 band to 42 in the 400-800 nm range. The following subsections describe the pre-processing algorithms applied to the images.

### 4.3.1 Image Pre-processing

*Atmospheric Correction*

The algorithm used to make atmospheric corrections to the images is called Tafkaa, a modified version of the ATREM algorithm and developed by the U.S. Naval Research Laboratory, Washington, DC. It basically calibrates imagery from the measured sensor radiance and transforms it to remote sensing reflectance. The main goal of this algorithm is to remove the confounding effects of the atmosphere. For the case of aquatic environments, the process of atmospheric corrections turns out to be more complex than for land, since varying effects of specular reflection, wind blown surface waves and reflectance from the benthic substrate are present in the measurements [1]. This software uses lookup tables to account for these aerosol types and gaseous scatterings and requires specifying latitude, longitude, time, aircraft altitude, relative humidity, aerosol type and aerosol optical depth, water vapor column amount, and winding speed [1, 25].

*Sunglint Correction*

When treating ocean scenes, it is not always sufficient to use atmospheric correction alone. There are wind-blown surface waves and specular reflection in the ocean surface that add extra brightness and artifacts to the entire image and specific areas. This problem is called sunglint. This problem can be treated because it can be analyzed as a function of the solar angle, surface conditions and the viewing geometry. If the flight conditions, time of the day and position are known, a majority of these effects can be corrected. To overcome this issue, a treatment called a 750 nm normalizing correction described in [4] was applied. It assumes that the necessary correction for each pixel is constant across all wavelengths. The equations that approximate remote sensing reflectance from the atmospherically corrected data are shown below and detailed in [1].

$$R_{rs}(\lambda) = R_{rs}^{raw}(\lambda) - R_{rs}^{raw}(750) + \Delta, \tag{4.1}$$

$$R_{rs}(\lambda) = R_{rs}^{raw}(\lambda) - R_{rs}^{raw}(750) + \Delta = 0.000019 + 0.1\left(R_{rs}^{raw}(640) - R_{rs}^{raw}(750)\right) \qquad (4.2)$$

### 4.3.2 Endmember Spectras

The endmembers represent the pure components of a scene. The goal of using these endmembers is to create linear approximation of the spectral signature measured by the sensor. In this study, three endmembers or classes were considered: sand, coral and algae. The endmember spectras were collected *in situ* in October 2001 and April 2002 by Goodman and Ustin at Kaneohe Bay in Hawaii. They were measured with a modified GER-1500 spectrometer [1]. Figure 4.2 shows these reflectances.

Due to strong light attenuation affecting wavelengths larger than 675 nm, this study was focused on the 400-675 nm range. However, the 550-675 nm range seems to provide better spectral separability and was tested in both [1] and this study. The algorithms compute the abundance estimates using data on this range only.

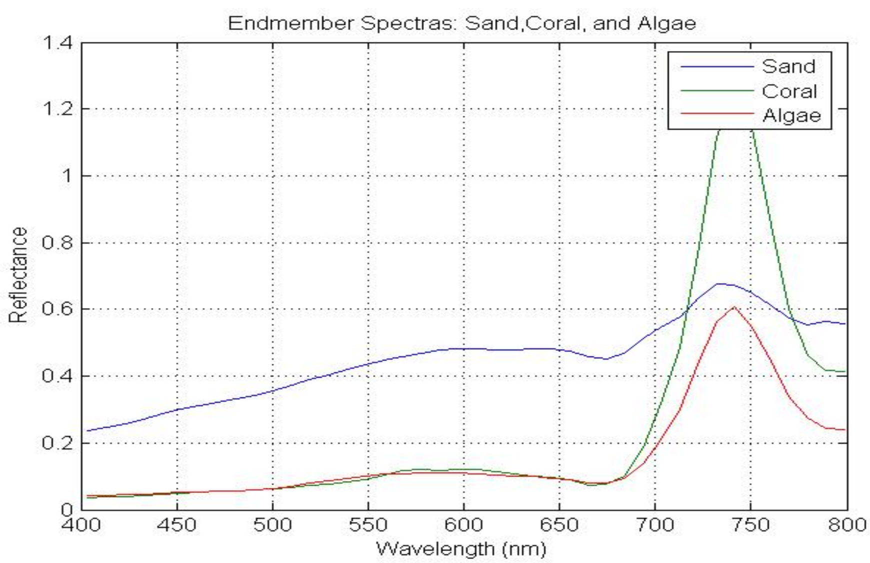


**Figure 4.1.** Endmember Spectras.

The abundance vector estimate $\hat{x}$ was obtained using a Nonnegative Sum to One algorithm (NNSTO), where the abundance fractions must sum to one and the must be equal or greater than zero. The Nonnegative Sum to Less or Equal to One (NNSLO) algorithm was also tested but provided poorer results. The NNSTO was the preferred algorithm to run the tests. For more details refer to Chapter 2 or [17, 29, 30].

### 4.3.3 Experiments with a Kaneohe Bay dataset

A small portion of the AVIRIS image of Kaneohe Bay is used to test the algorithms with actual airborne hyperspectral data. It consists of a 50x50 pixel area, already corrected for atmospheric and sunglint effects. Because they were not measured at the time of the AVIRIS data acquisition, there is no way of knowing the exact values for B, BP, G and P. However, water depth estimates from the SHOALS are available and are used to compare the estimates obtained with the algorithms with those measured by this instrument. The agreement of the depth estimates with SHOALS measurements was used as a measure of model performance for our approach.

*Scanning Hydrographic Operational Airborne Lidar Survey (SHOALS)*

SHOALS uses short pulses of light to detect water depth, one at an infrared wavelength to detect the water surface and other at the blue-green wavelength to detect the bottom, 1064 nm and 532 nm respectively. The aircraft is positioned via GPS systems, providing vertical positioning accuracy of ± 15 cm and ± 1m of horizontal positioning, and a depth accuracy of ± 15 cm. It operates at an altitude of 400m at a speed of 50 to 70 m/s, giving an elevation measurement every 8 m with a scan swath width of 220 m. This system not only provides depth measurements but also collects geo-referenced video with the lidar measurements, which is used to position objects like piers or navigation aids [33]. The area of Kaneohe Bay that has been processed with SHOALS measurements is used in this chapter for accuracy assessment of the depth estimates.

Results obtained for the OP's, depths, and the abundance estimates are shown below. They are presented as colormaps, where the blue values are the lowest, and the red values are the highest. Refer to Table 2.2 if needed as a reference for the parameter definitions. We compare both new methods based on each of the parameters as well as the benthic mapping. These two methods will also be compared with the results obtained by Goodman's implementation.

Before putting these algorithms through this dataset, they were tested with other small 25x25 subsets of AVIRIS pixels that individually contain sand, coral or algae to see if the abundance estimates were correct. These small datasets were regions in the Kaneohe Bay where the bottom composition is known. Table 4.7 shows the abundance value obtained for each material for a given pixel on both the CIUB and CIUS algorithms.

**Table 4.7.** Abundance estimates for sand, coral and algae datasets

| Pixel # | Sand dataset | | Coral dataset | | Algae dataset | |
|---|---|---|---|---|---|---|
| | CIUB | CIUS | CIUB | CIUS | CIUB | CIUS |
| 1 | 1 | 1 | 0 | 0 | 0.8537 | 0.8461 |
| 2 | 1 | 1 | 0.6595 | 0.7276 | 0.8810 | 0.9021 |
| 3 | 1 | 1 | 0.7036 | 0.7379 | 0.8429 | 0.8457 |
| 4 | 1 | 1 | 0.7315 | 0.7593 | 0.7522 | 0.7613 |
| 5 | 1 | 1 | 0.7360 | 0.7789 | 0.8467 | 0.8401 |
| 6 | 1 | 1 | 0.1091 | 0.6841 | 0.7339 | 0.7418 |
| 7 | 1 | 1 | 0.7304 | 0.7815 | 0.7888 | 0.7901 |
| 8 | 1 | 1 | 0.7061 | 0.7375 | 0.8160 | 0.8126 |
| 9 | 1 | 1 | 0.6919 | 0.7196 | 0.7647 | 0.7703 |
| 10 | 1 | 1 | 0.7414 | 0.7716 | 0.7389 | 0.7497 |
| 11 | 1 | 1 | 0.6360 | 0.6866 | 0.6718 | 0.6898 |
| 12 | 1 | 1 | 0.7127 | 0.7448 | 0.7556 | 0.7618 |
| 13 | 1 | 1 | 0.7145 | 0.7398 | 0.7432 | 0.7524 |
| 14 | 1 | 1 | 0.7210 | 0.7394 | 0.7451 | 0.7527 |
| 15 | 1 | 1 | 0.7124 | 0.7414 | 0.7737 | 0.7808 |
| 16 | 1 | 1 | 0.5865 | 0.6864 | 0.6807 | 0.6969 |
| 17 | 1 | 1 | 0.6637 | 0.7277 | 0.6799 | 0.6963 |
| 18 | 1 | 1 | 0.6616 | 0.7000 | 0.7061 | 0.7196 |
| 19 | 1 | 1 | 0.6993 | 0.7367 | 0.7451 | 0.7527 |
| 20 | 1 | 1 | 0.7268 | 0.7650 | 0.7833 | 0.7852 |
| 21 | 1 | 1 | 0.5799 | 0.6782 | 0.6262 | 0.6446 |
| 22 | 1 | 1 | 0.6800 | 0.6969 | 0.6537 | 0.6720 |
| 23 | 1 | 1 | 0.6977 | 0.7221 | 0.6057 | 0.6300 |
| 24 | 1 | 1 | 0.6828 | 0.7193 | 0.6235 | 0.6430 |
| 25 | 1 | 1 | 0.6828 | 0.7193 | 0.6412 | 0.6606 |

*Remote Sensing Reflectance Estimation*

Observing the pictures below, the estimates best matching the measured remote sensing reflectance is CIUB method. Red regions indicating algae are almost similar in LIGU and the one shown in figure 4.4b, but not as close as CIUB. The figure 4.4c illustrating the results from CIUS shows that fewer algae were estimated and probably an overestimation of sand occurred.

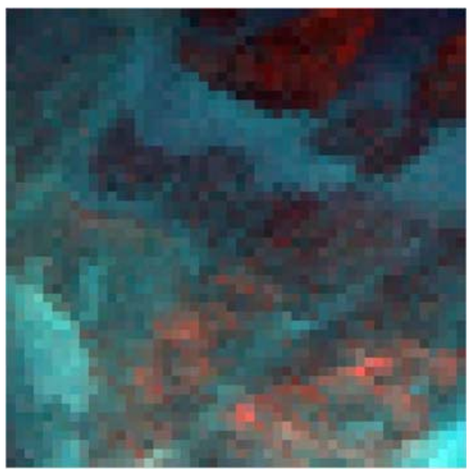

**Figure 4.2.** RGB composite of AVIRIS dataset (R=703.07nm, G=539.10nm, B=500.41nm).

The circled area is to highlight the brightness appearing on the AVIRIS image, and the most similar in this detail, is the CIUB algorithm.

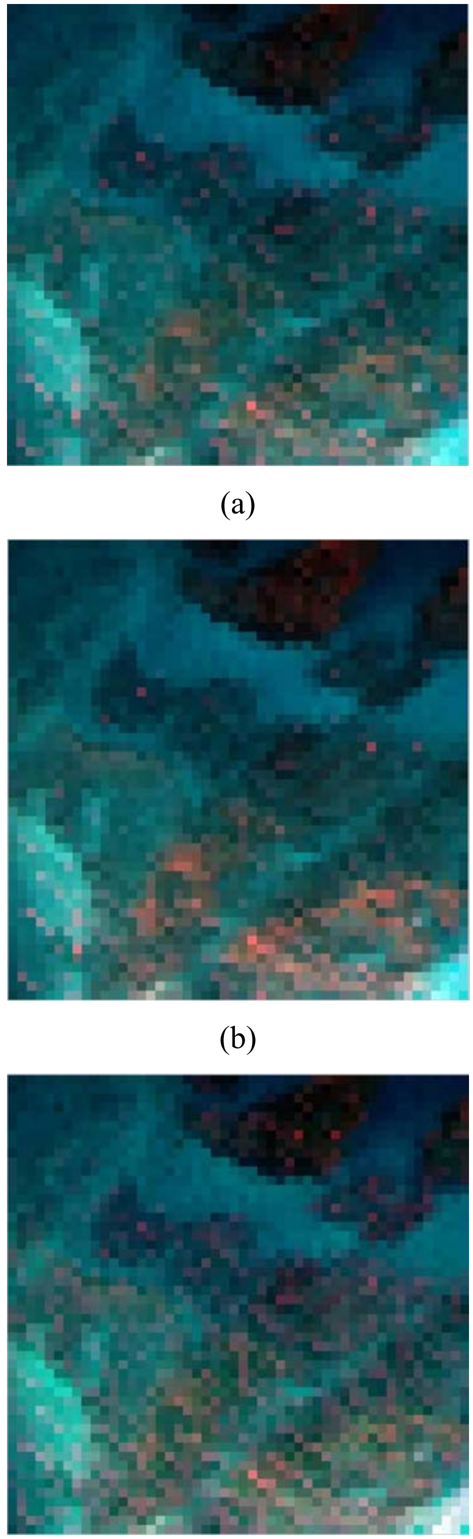

(a)

(b)

(c)

**Figure 4.3.** Estimated RGB (R=703.07nm, G=539.10nm, B=500.41) composites of the scene. $R_{rs}$ estimates of (a)LIGU (b) CIUB (c) CIUS

*Comparison of fitting errors*

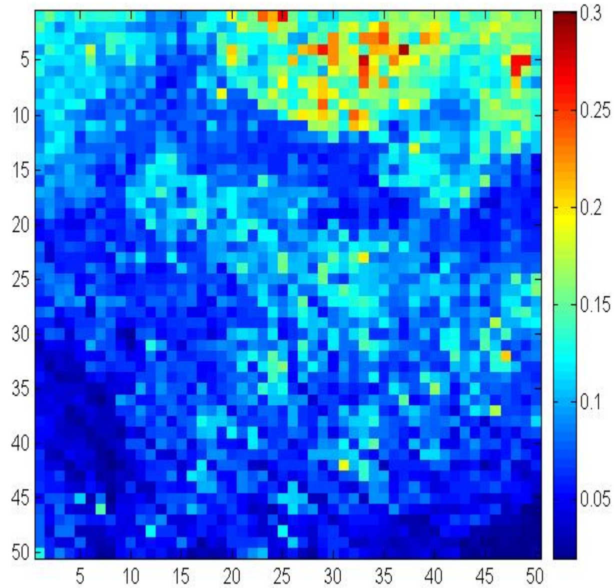


**Figure 4.4.** Fitting error image scaling for LIGU

Before presenting the fitting errors on CIUB and CIUS, is important to mention that the minimization of the error in CIUB approach is in terms of subsurface remote sensing reflectance while LIGU and the CIUS approach minimizes the error of remote sensing reflectance. For that reason, the estimated subsurface remote sensing reflectance in the bottom surface approach was converted to surface remote sensing reflectance and an error was calculated, thus making the three approaches comparable.

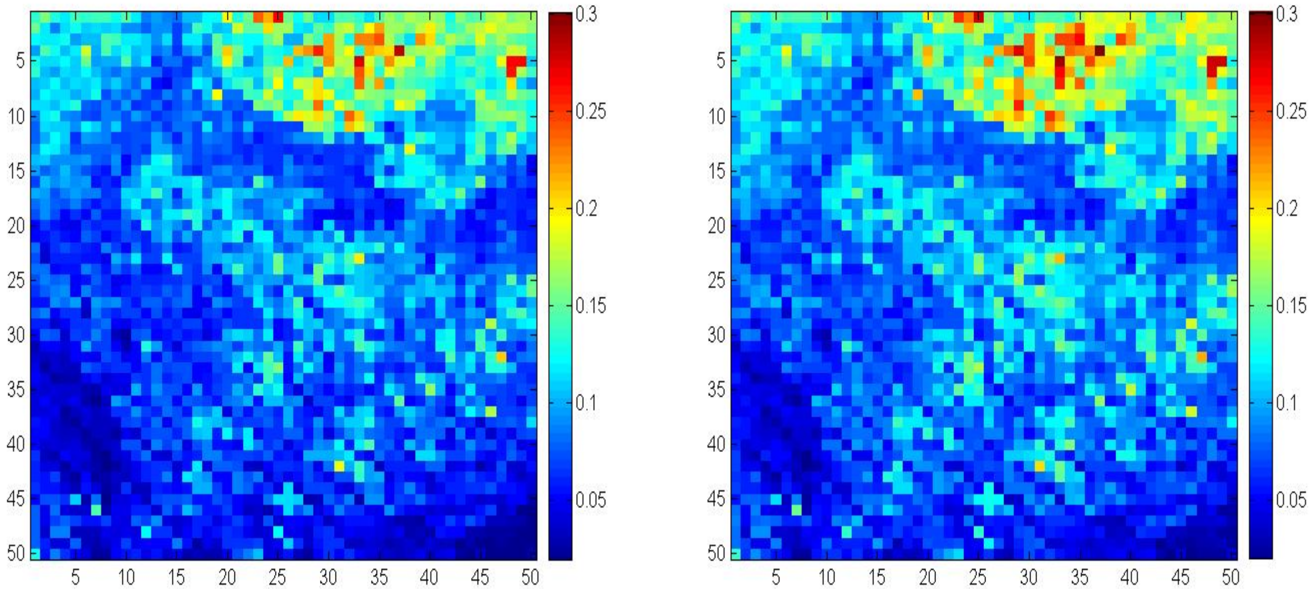


(a) (b)

**Figure 4.5.** Image scale of fitting errors for (a) CIUB (b) CIUS.

Fitting errors to the remote sensing reflectance curves look acceptable at least when compared with LIGU. There seems to be the greater fitting errors at the right upper part of the dataset, where red values appear showing errors of about 30%. The pixels in red appear to be almost the same on the three images. Since these images do not show any visible differences, let us take a look at the histograms of the errors and compare them by statistics like mean and variance. As mentioned before, these errors calculated are all based on remote sensing reflectance rather than subsurface remote sensing reflectance.

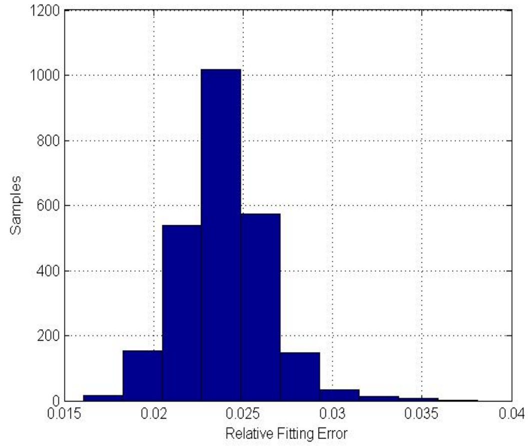


(a) Mean=0.0239; Variance=5.7351e-006

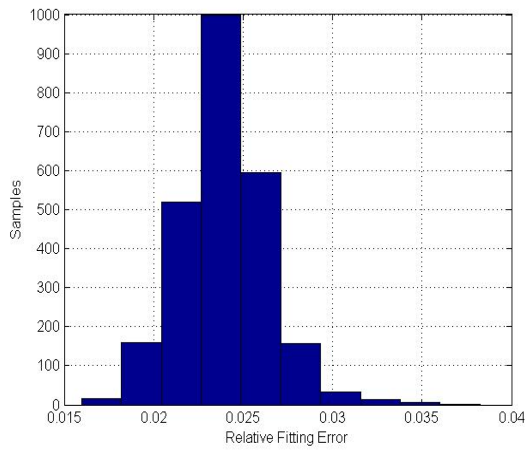


(b) Mean=0.0239; Variance=5.8673e-006

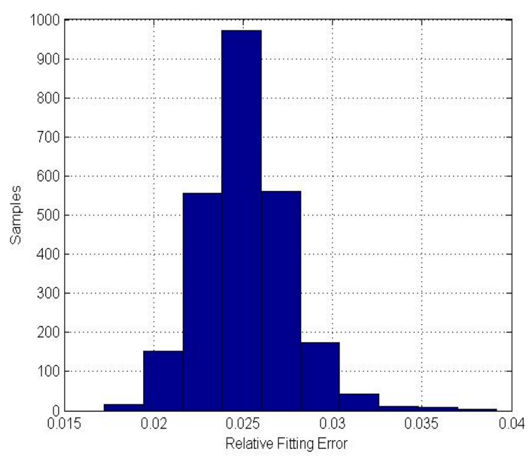


(c) Mean=0.0251; Variance=6.2286e-006

**Figure 4.6.** Fitting Error Histograms (a) LIGU (b) CIUB (c) CIUS (remote sensing reflectance).

LIGU and CIUB have very close mean and variance. The CIUS algorithm did not performed as well.

*Depth Estimates*

Both the CIUB and LIGU are very close in accuracy, whereas the CIUS is slightly less accurate. Another avenue for comparing the different methods is to use water depth estimation, which is available from SHOALS data. A good way of visualizing this data is to look at scatter plots of the measured SHOALS data vs. the estimated H.

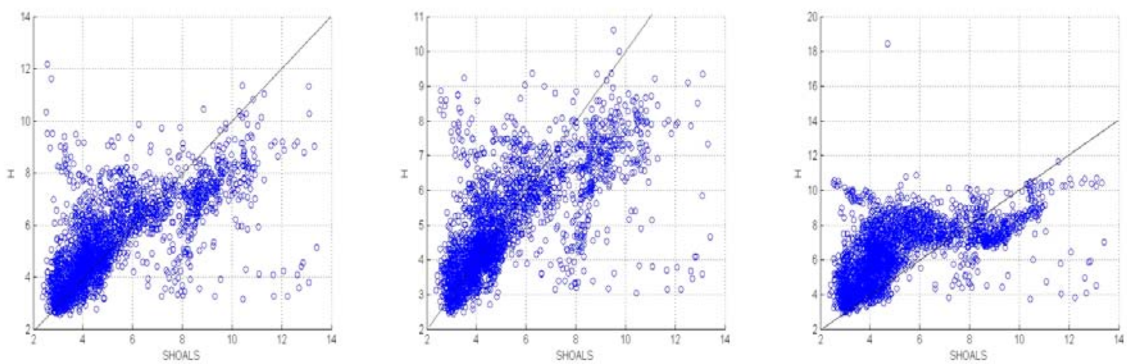


(a) m=0.8891; b=0.4694 (b) m=0.9806; b=0.2892 (c) m=0.7045; b=0.6942

**Figure 4.7.** Scatter plots of depths (a) LIGU, (b) CIUB, (c) CIUS. (meters)

Linear regression analysis was conducted and may be expressed as:

$$H_{SHOALS} = m\hat{H} + b \tag{4.3}$$

where $\hat{H}$ is the depth estimate, m is the slope, and b the y-intercept. In theory, it is desirable to obtain an m=1 and a b=0 to make a 1-to-1 relationship, but this obviously not possible when dealing with real data, so at least we want this values to be as close as possible to 1 and 0 respectively.

Excellent results were attained for water depths estimates with CIUB, the method that does the unmixing at the bottom of the surface with slope very close to 1. The second best was LIGU, and third, again, the CIUS approach. It is observable that estimates in water depths are very good shallower than five meters. Notice the relation in fitting error and water depth as the water depth increases. It is especially noticeable at the upper right corner of the images. When looking at Figure 4.9, the deepest waters are located in that area and the highest fitting errors are too. Now the colormaps of the water depth will be shown as well as the rest of the OP estimates, and abundance estimates. Again, because they were not measured at the time of the AVIRIS acquisition, there is no way of knowing the true values for these parameters (i.e. there are no *in situ* measurements are available for this data set).

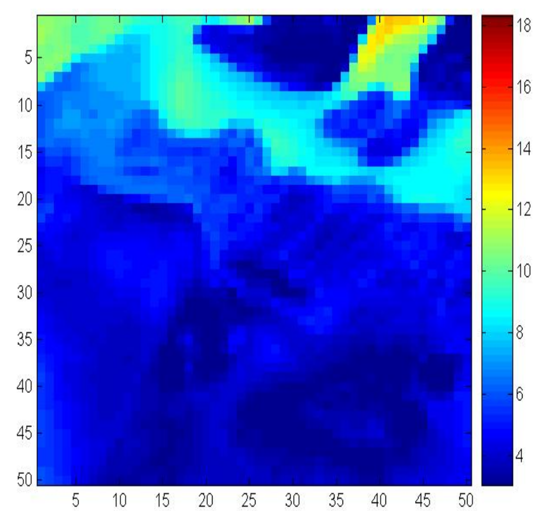


**Figure 4.8.** Water depth measurements from SHOALS. (meters)

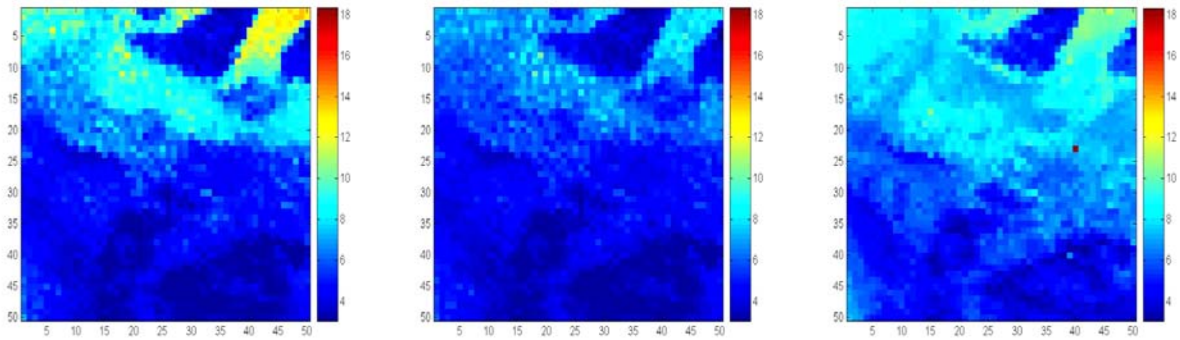

(a) (b) (c)

**Figure 4.9.** Water depth (in meters) estimates for (a) LIGU (b) CIUB (c) CIUS. (meters)

Visually, it seems that the LIGU obtained better depth estimates, then by the CIUS and by the CIUB. When looking at the shallower areas, both the LIGU and CIUB look very similar as compared to SHOALS.

The next figure shows histograms of the relative difference between the SHOALS's measurements and the estimated depths. The CIUB is slightly superior (in terms of mean and variance) than the LIGU approach, and once again the CIUS method has the lowest performance.

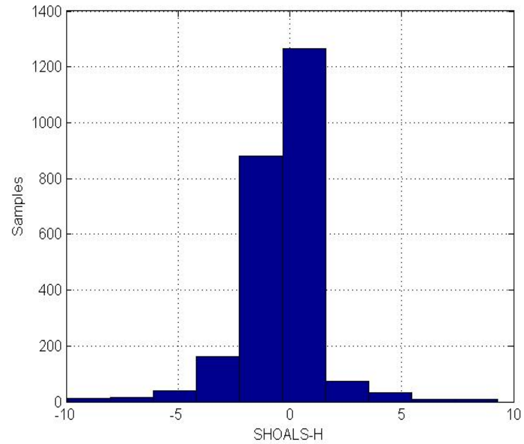


(a) Mean=-0.4030; Variance=2.9698 (in meters)

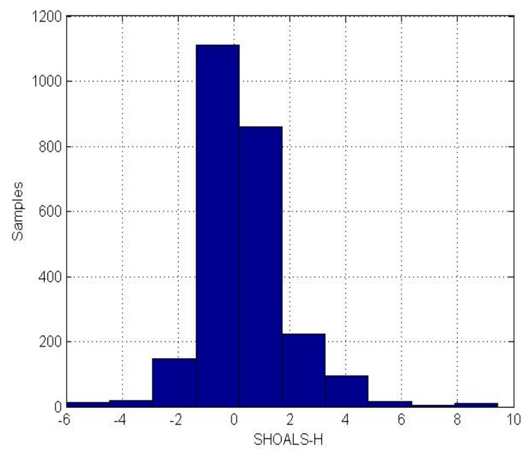


(b) Mean=0.3385; Variance=2.3367 (in meters)

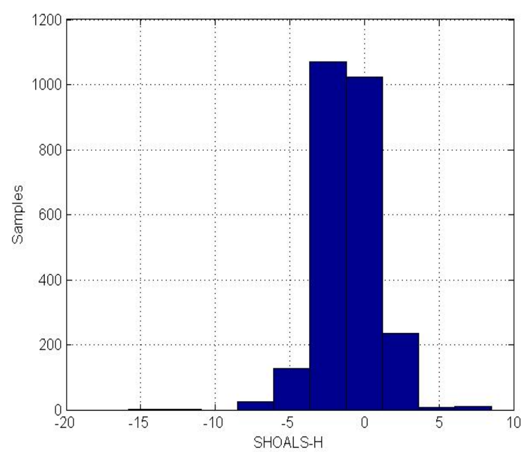


(c) Mean=-1.1818; Variance=3.2941 (in meters)

**Figure 4.10.** Depth Error Histograms(a)LIGU (b) CIUB (c) CIUS

*Parameter B*

The parameter B estimates will be compared with just two methods since the unmixing at the surface method does not uses B for the estimation of the remote sensing reflectance due to the structure of the modeling approach.

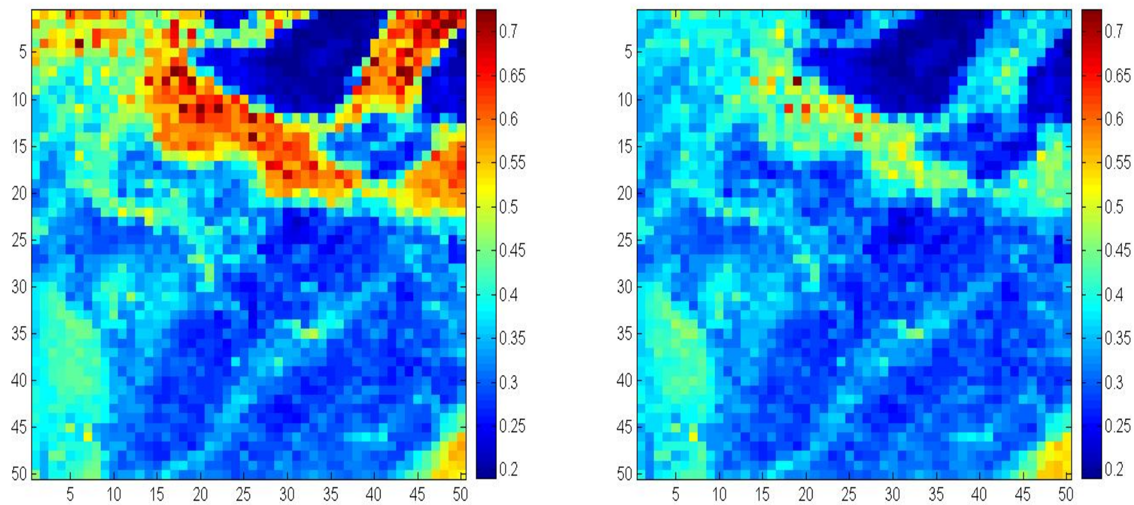

(a) (b)

**Figure 4.11.** B estimates for (a) LIGU (b) CIUB

There is a slight difference in these two images, there seems to be higher estimates of B for Goodman's approach in certain areas of the data set.

*Parameter BP*

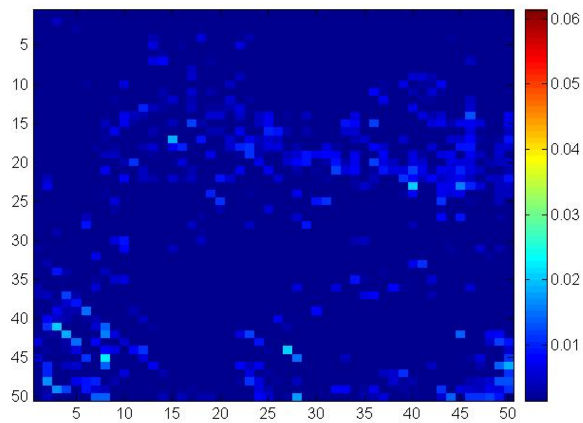

**Figure 4.12.** BP estimate from LIGU.

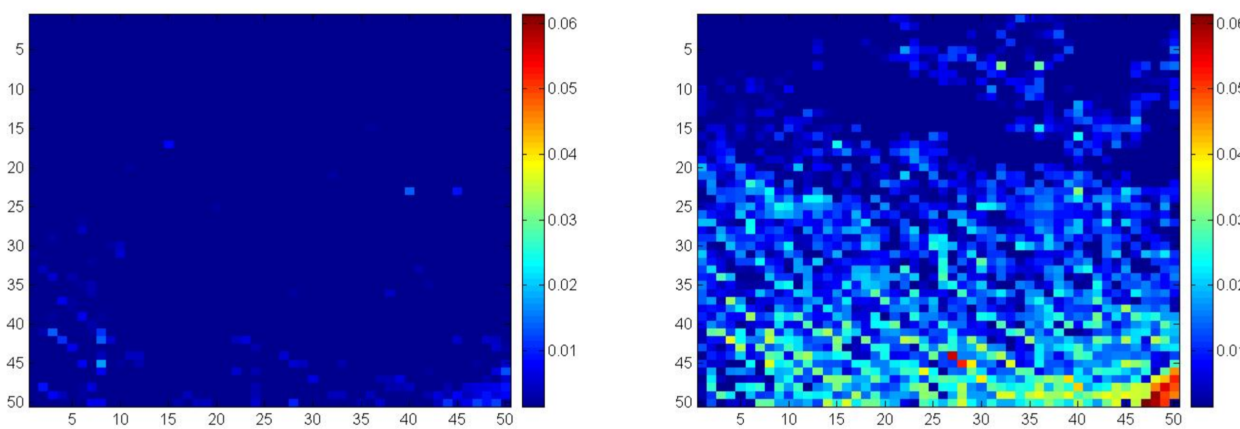

(a) (b)

**Figure 4.13.** BP estimates for (a)CIUB (b) CIUS

Similar values of BP were obtained by both LIGU and CIUB approaches. More varying values ranging from 0.0001 to 0.06 were obtained by the CIUS approach. This is something that obviously gives more credibility to the first two approaches stating that water properties should be more homogeneous in such a small area.

*Parameter G*

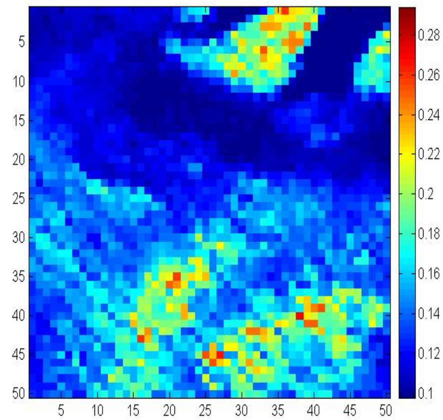


**Figure 4.14.** G estimate LIGU.

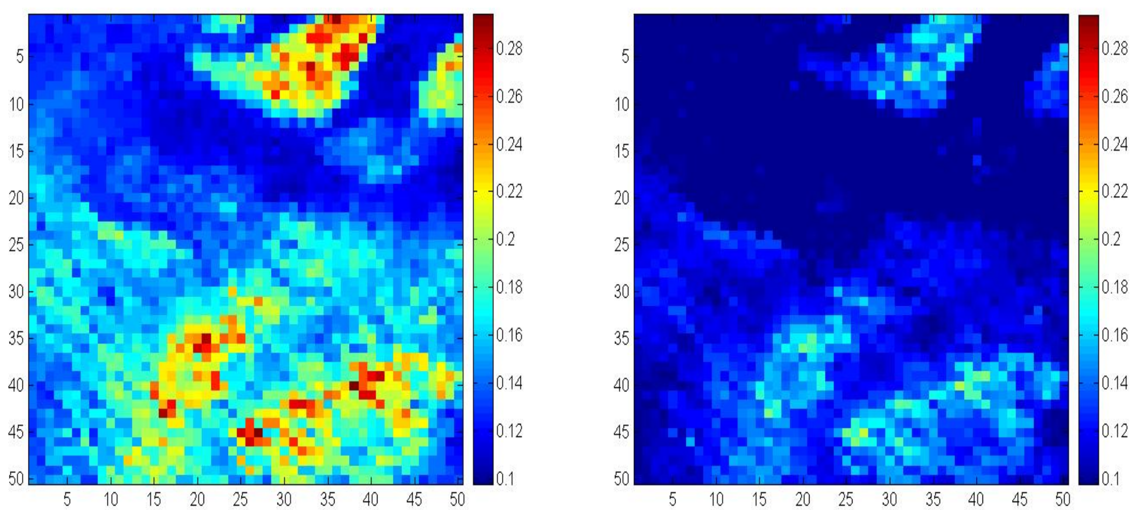


(a) (b)

**Figure 4.15.** G estimates for (a) CIUB (b) CIUS.

Estimates of G obtained by the LIGU and the CIUB approaches were similar, which in both cases is higher than the estimates from the CIUS approach. Note the dependence on the bottom characteristics. This is one thing that should be further studied since, as seen with simulated pixels, the G parameter describes absorption of gelbstoff and detritus, found in the water column, not the bottom of the ocean.

*Parameter P*

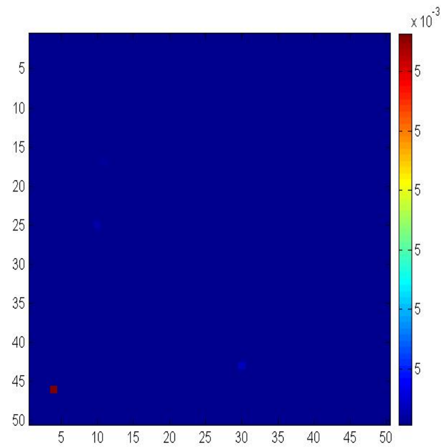

**Figure 4.16.** P estimate from LIGU.

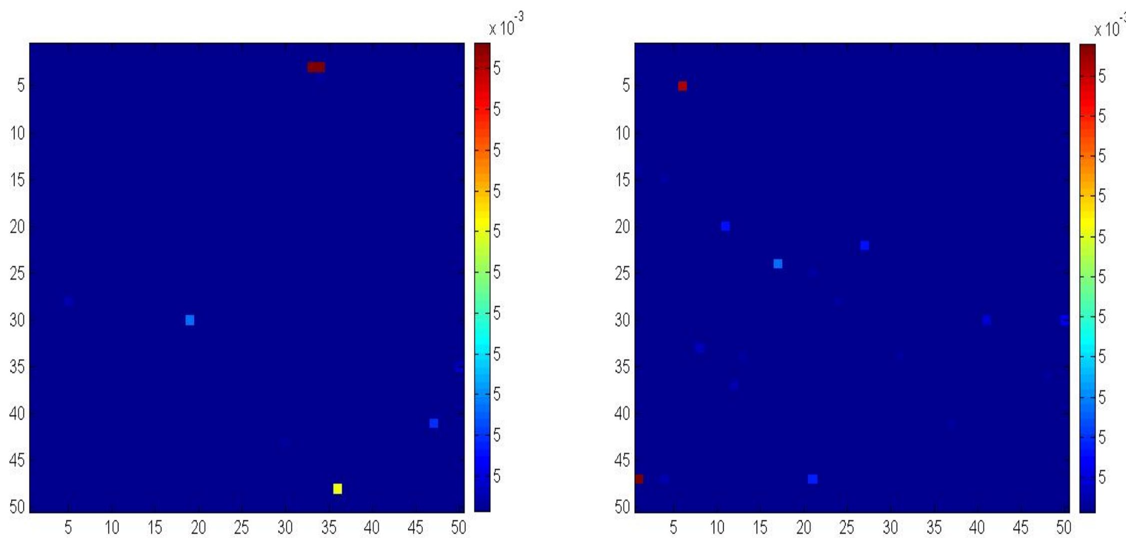

(a) (b)

**Figure 4.17.** P estimates for (a)CIUB (b) CIUS

The three approaches look very similar; almost all the pixels got estimates of 0.005, the lower limit of this parameter. The optimization routine in the three approaches is able to do the curve fitting by making this value as small as possible.

*Abundance Estimates*

An RGB composite of the dataset is displayed for each of the methods. The red band corresponds to coral, the green to algae, and the blue to sand.

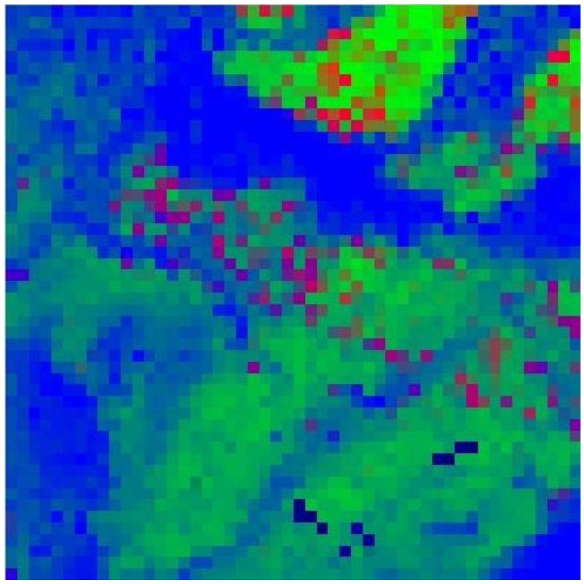

**Figure 4.18.** Abundance map. LIGU.

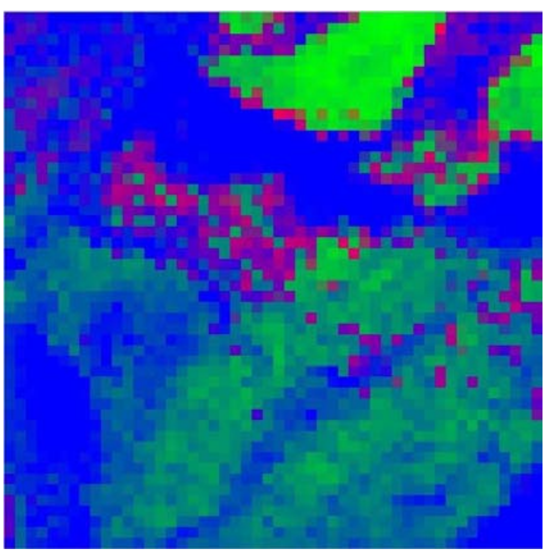

(a)

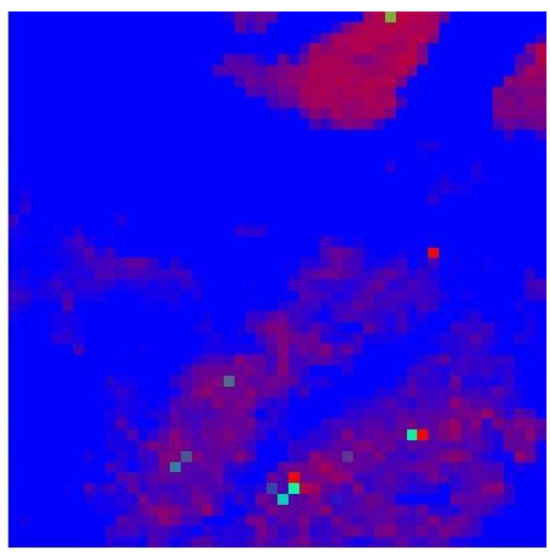

(b)

**Figure 4.19.** Abundance estimates for (a) CIUB (b) CIUS.

As observed, the calculation of optical properties at the bottom or at the surface, by using one of the two new approaches clearly affects the estimation of abundance estimates. This clearly states that the algorithm that both the CIUB and the LIGU are probably more reliable, at least in this dataset, were water depths ranged from 2 to 13 meters.

Now, an image for each abundance map for each endmember is shown for each for the CIUB, CIUS and LIGU.

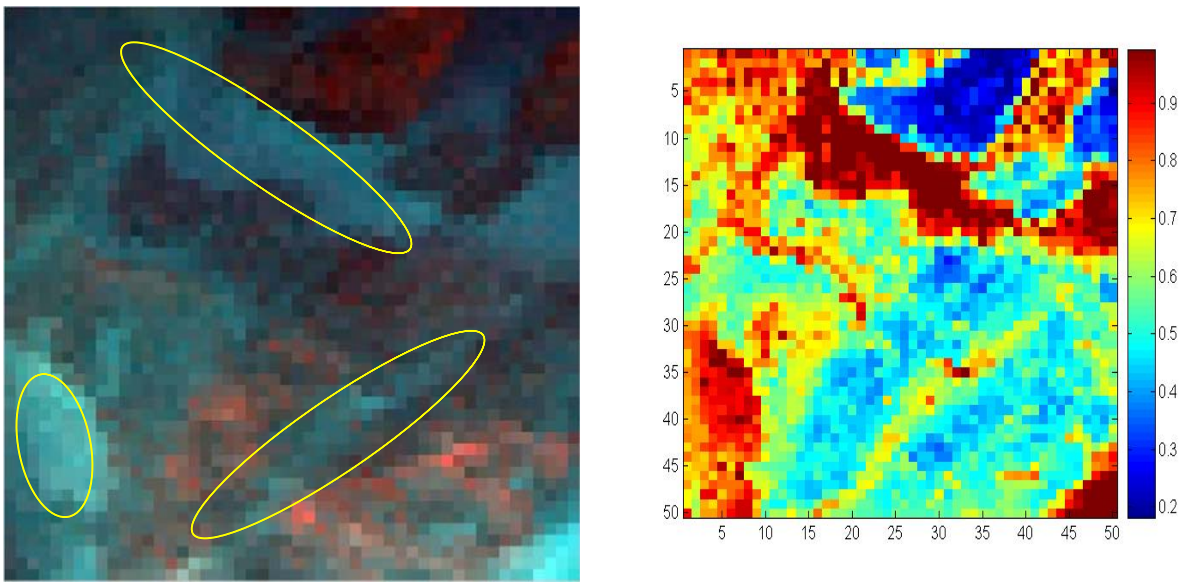


(a) (b)

**Figure 4.20.** (a) RGB of AVIRIS dataset (b) Sand estimates for LIGU.

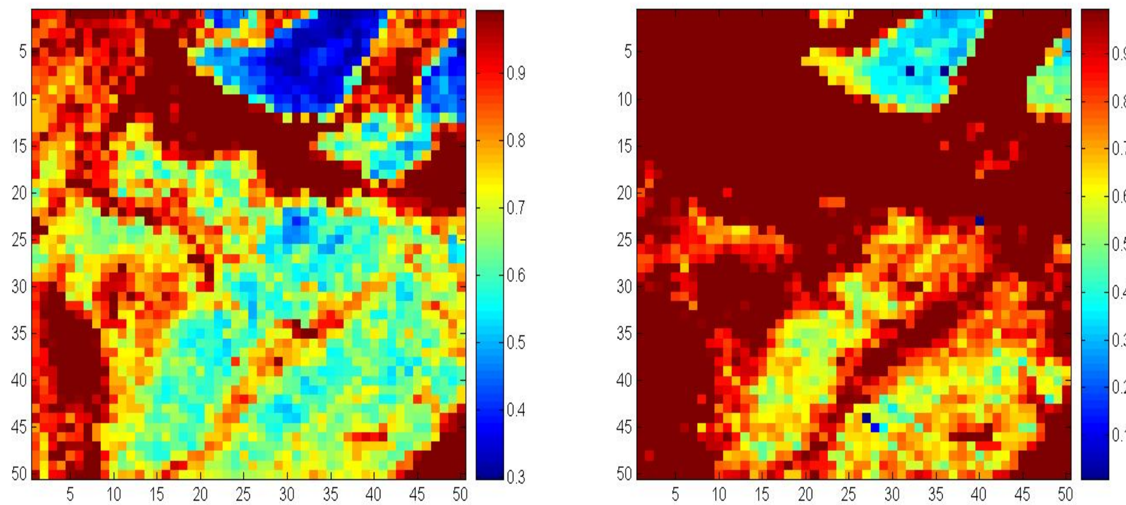

(a) (b)

**Figure 4.21.** Sand estimates for (a) CIUB (b) CIUS.

There is a diagonal line of sand at the second lower half of the image, which is more defined in the CIUB than the LIGU. CIUB and CIUS have more solid coloring on sand.

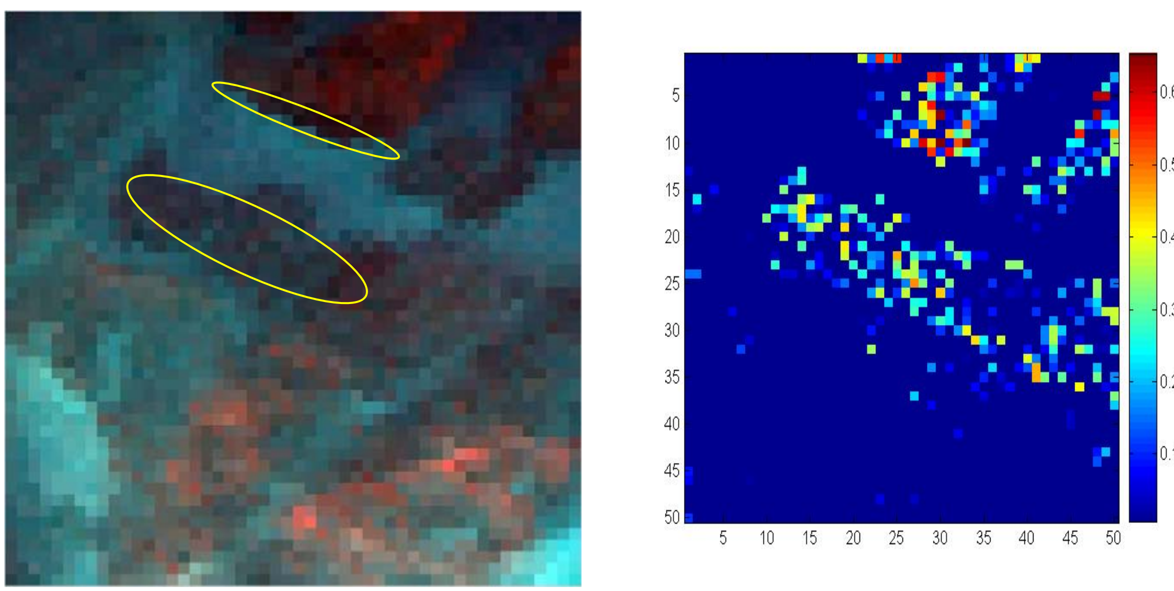

(a) (b)

**Figure 4.23.** (a) RGB of AVIRIS dataset (b) Coral estimates for LIGU.

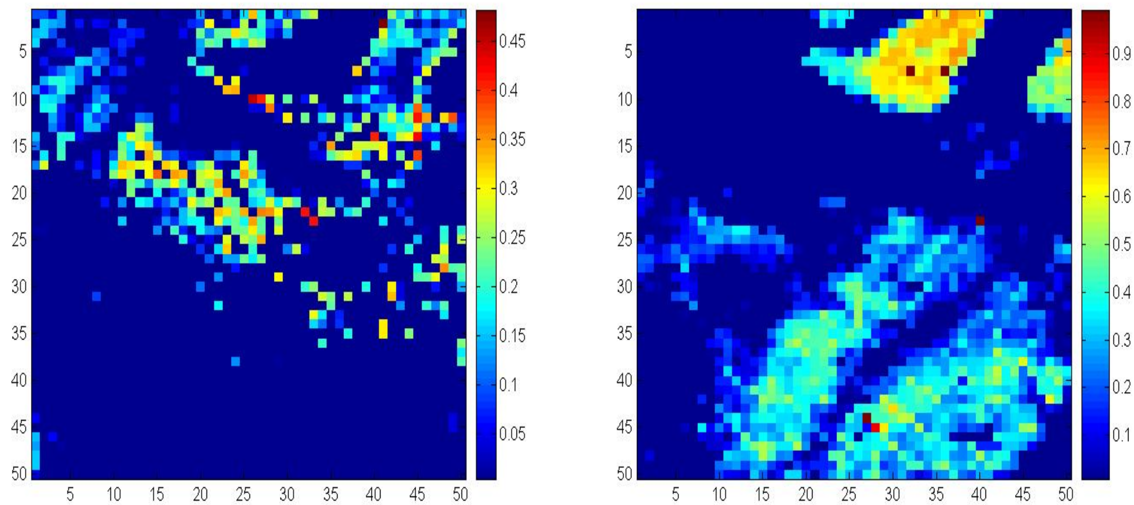


(a) (b)

**Figure 4.23.** Coral estimates for (a) CIUB (b) CIUS.

Circled regions on the RGB of the AVIRIS dataset shows there is more definition of what could be coral on the CIUB than on the LIGU.

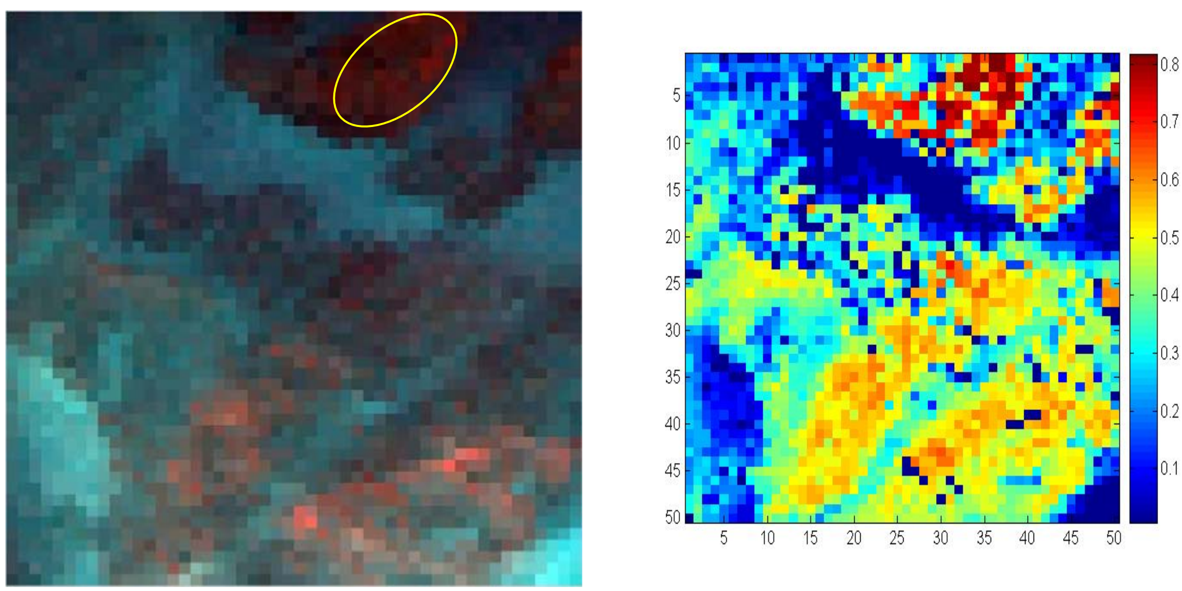


(a) (b)

**Figure 4.24.** Algae estimate. LIGU.

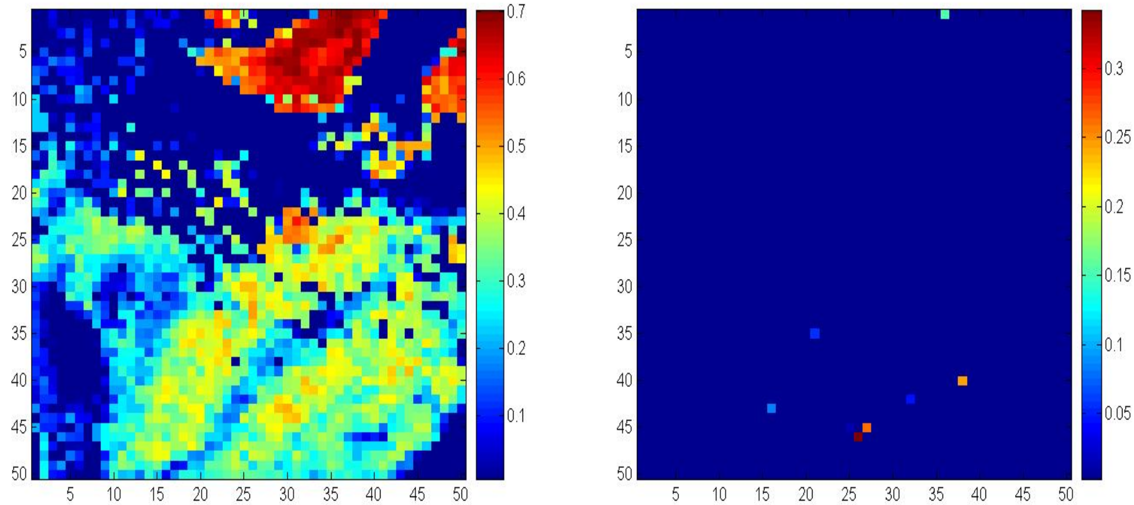


(a) (b)

**Figure 4.25.** Algae estimates for (a) CIUB (b) CIUS.

Coloring of algae is more homogenous in the CIUB as compared to the LIGU, while there is basically no algae estimation with CIUS.

## 4.4 Summary and Conclusions

In this Chapter, we tested, validated and compared the algorithms described in Chapter 3 were effectuated. First, each approach was tested with simulated pixels for both clear and optically dense waters, and noticed that good depth estimates were obtained for up to 20 meters depth in clear water and around 5 meters depth for optically dense waters. For very clear waters, good abundance estimates were obtained up to water depths of 15 meters, whereas above 2 meters of optically dense water affected the abundances, producing an overestimation of coral. Also abundance estimates were slightly better with the CIUB algorithm for both clear and optically dense pixels. Parameters BP, G and P seemed to be less dependable on water depth and optically denseity, since good estimations were obtained with very high depths, in both optically dense and clear waters. The algorithms were also tested with real data from a dataset of an image taken from AVIRIS of the Kaneohe Bay, and the algorithm that performs the unmixing at the bottom of the surface seemed to be superior to that making the unmixing at the water surface. When compared to Lee's Inversion and Goodman's linear mixing model, it worked very close in terms of curve fitting to the $\boldsymbol{R_{rs}}$ measurement, and slightly superior depth estimates when compared to SHOALS measurements. Abundance estimates were more consistent in areas where dense sand paths or coral or algae concentrations looked very homogeneous when looking at the AVIRIS RGB composite.

# Chapter 5

# Application to Kaneohe Bay

## 5.1 Introduction

In this chapter, an AVIRIS hyperspectral image from the Kaneohe Bay, Hawaii will be processed by the CIUB algorithm. This area is good to demonstrate our approach since it has a low diversity of coral species and benthic life, but at the same time has a wide range of areas that can be classified. These areas include optically dense waters, coral reefs at different water depths, algae colonies and sand sites. The main purpose of processing this image is to obtain estimates of water properties, bathymetry and benthic composition, which can be further contrasted with SHOALS measurements. Another important advantage is that in situ data and a dense quantity of information regarding the environmental properties of the scene is available, thus facilitating the process of validation [1].

## 5.2 Scene Description

Kaneohe Bay is located on the northeast shore of Oahu, Hawaii (Figure 5.1). It is basically an enclosed area of approximately 13 km long and 4 km wide. It contains several types of coral reefs like protecting barriers and patch reefs [24]. It is influenced by both freshwater and saltwater inputs. This freshwater, which originates from streams contributes sedimentation and pollutants, mostly due to urban development, deforestation and grazing. *Porites compressa* and *Montipora capitata* are the most abundant coral species. Algae species like the green bubble algae influenced coral reef displacement and contribute to coral reef decline. This is due to human related factors such as sewer inputs and pollutants due to urbanization, etc.


**Figure 5.1** The Oahu Island, Hawai.

Other advantages of studying the Kaneohe Bay include the available historic scientific literature describing the coral reef ecosystem, bathymetric charts, researches involving coral reefs monitoring, preservation and species identification. This facilitates the validation of algorithms using remote sensing techniques.

## 5.3 Parameter and Abundance Extraction

The algorithm used to analyze the whole scene of Kaneohe Bay was the algorithm that applies a mixing model at the bottom of the surface (CIUB). Results will be shown below. The RGB composite of this AVIRIS image is showed in the next figure next to an IKONOS's image for comparison. The AVIRIS image is atmospherically and sunglint corrected. The black areas surrounding the bay and some spots over water are a mask for clouds, land or off shore regions. These black areas were not run through the model. Following these two RGB images, estimation of abundances, water depths and the nuisance parameters BP, P and G will be shown in color map scales.

(a)

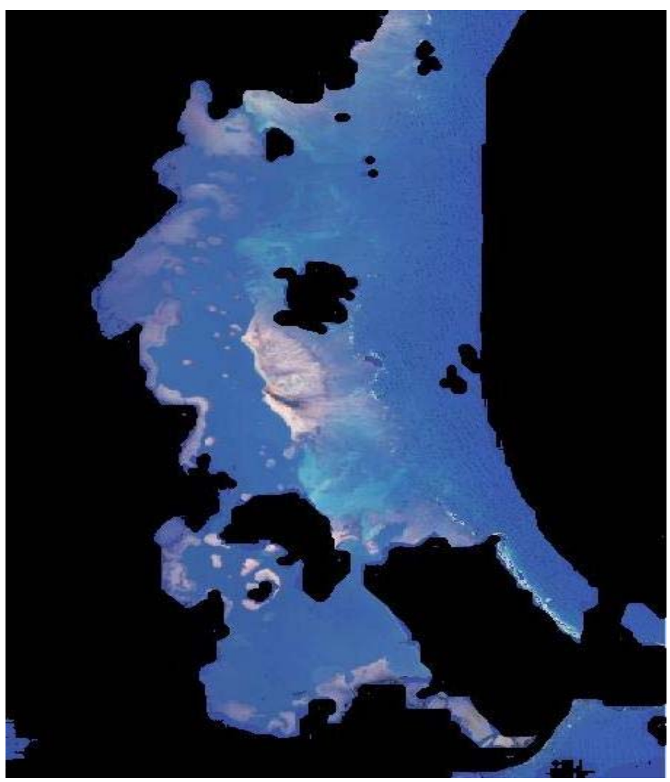

(b)

**Figure 5.2** Kaneohe Bay: RGB composite from (a) IKONOS (b) AVIRIS

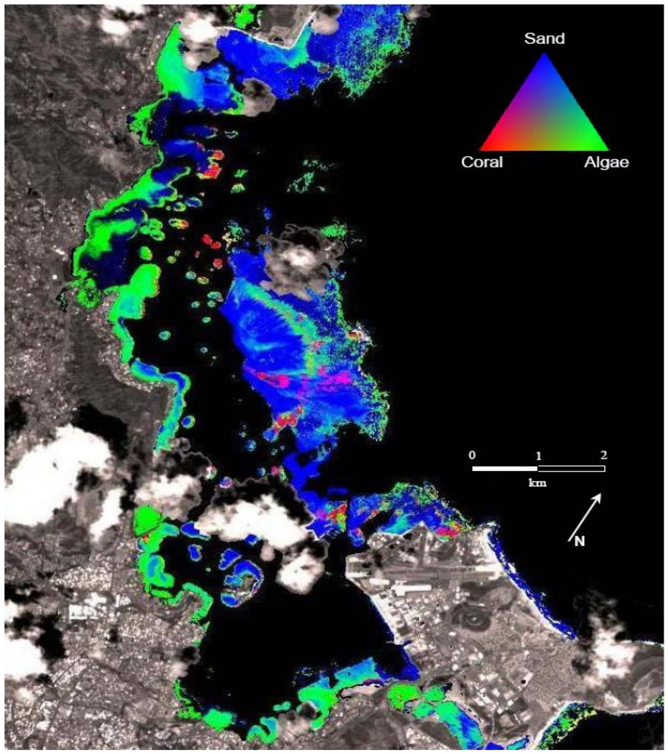


(a)

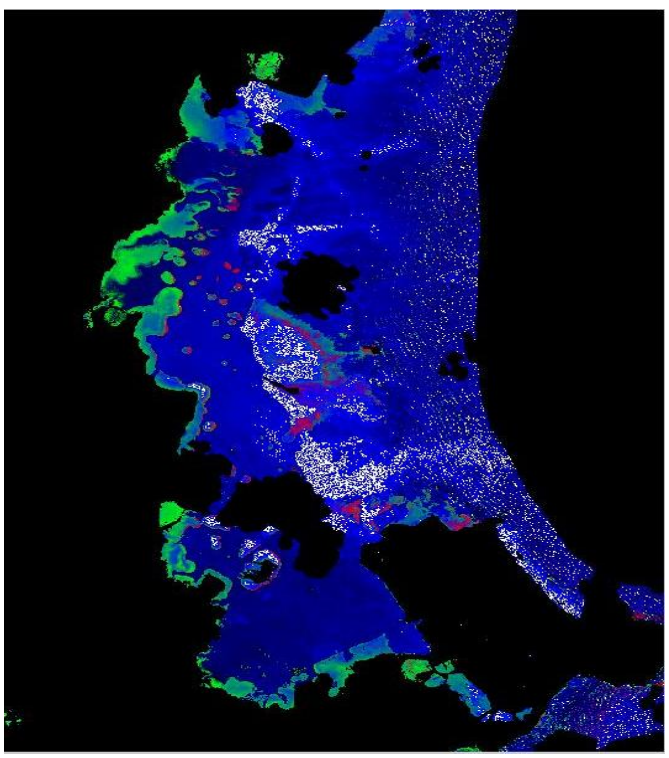

(b)

**Figure 5.3.** Abundance Colormap of Kaneohe Bay. Red for coral, green for algae and blue for sand. (a) Goodman Dissertation (b) CIUB

The abundance color map for the CIUB results shows several overestimations of coral reef in regions which are optically dense or very deep waters. This makes sense when taking a look to Figure 5.3 and noticing several red spots standing for errors in the curve fits very close to 1. There are more sand estimates in the CIUB results image since Goodman's colormap was masked with black for water depths above the three-four meters depths. In general, there is some congruence in the estimates for both algorithms. There is no way of making sure all the estimates are correct except for a few areas that were ground truth is available.

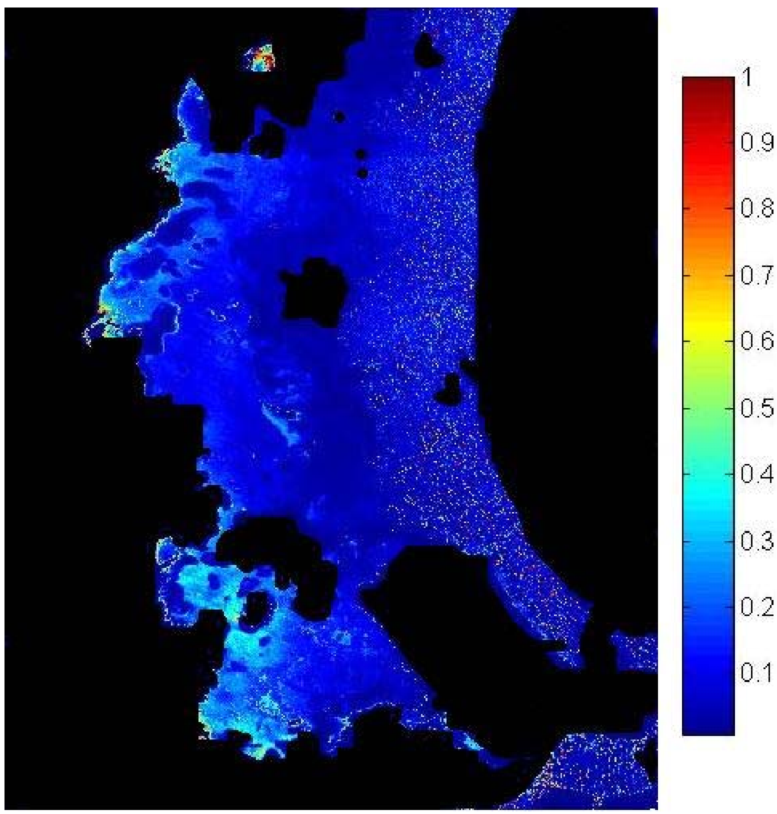


**Figure 5.4** Fitting error image.

The curve fitting errors mostly occurred in regions were very deep water is present, or muddy bottoms near the coast. These results agree with the results obtained with synthetic data, where sand was overestimated as the water depths increased, especially in optically dense waters. Also, one may observe that when the water depths estimates were above the 8-10 meters, coral overestimations were obtained in some regions, and at the same time with higher fitting errors.

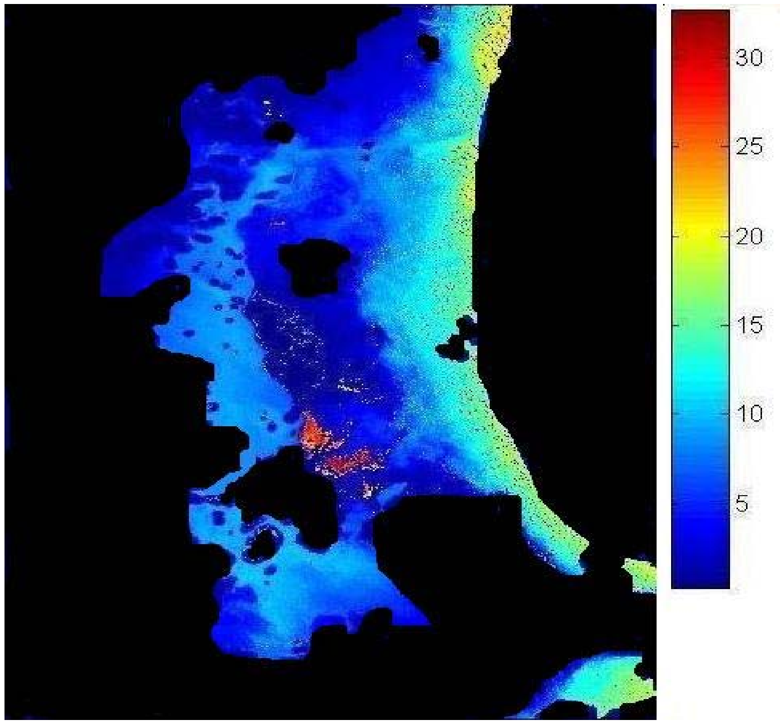


**Figure 5.5.** Depth estimate (H).

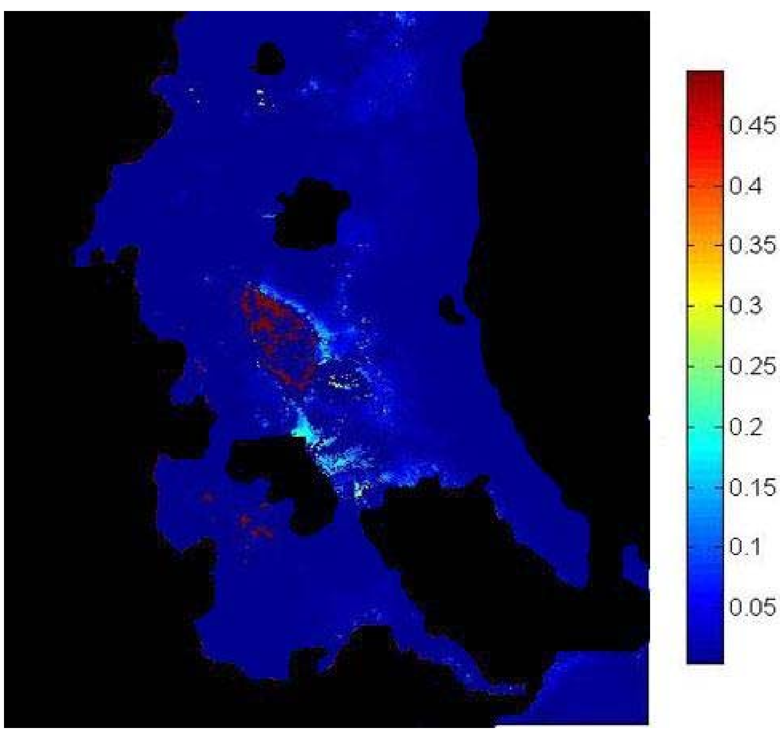


**Figure 5.6.** Estimate of BP.

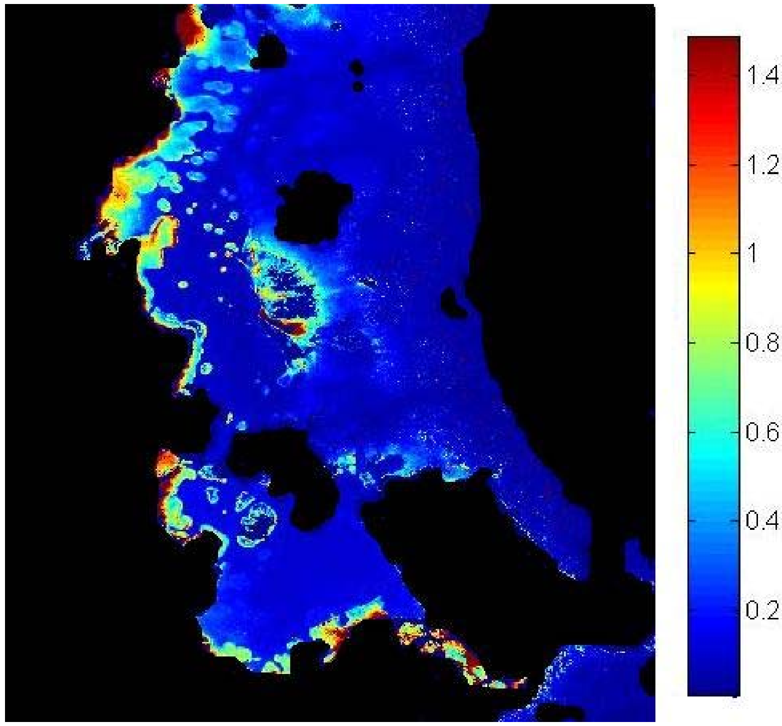

**Figure 5.7.** Estimate of G.

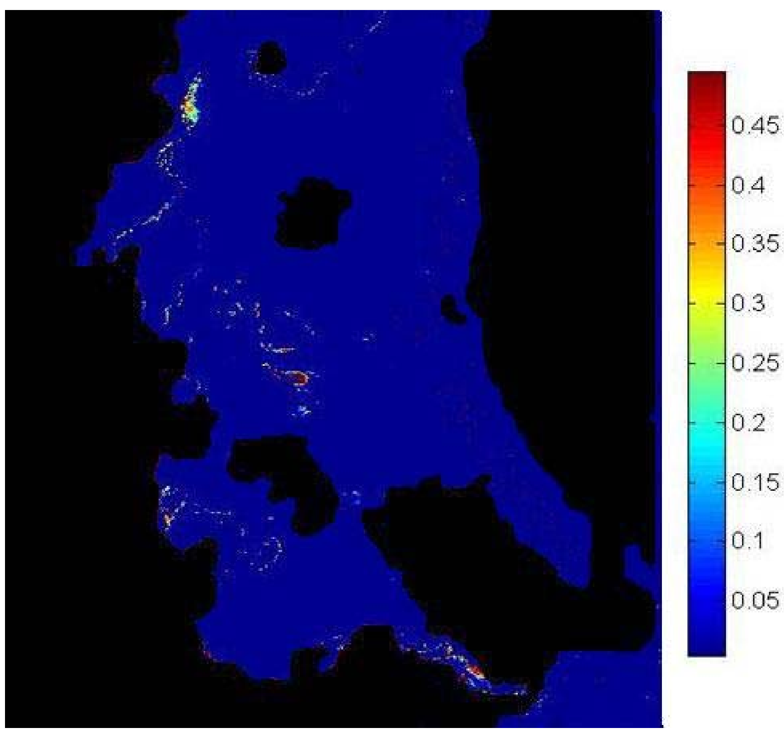

**Figure 5.8.** Estimate of P

## 5.4 Conclusions

The algorithm that applies a linear mixing model at bottom of the surface seems to be able to provide good fittings to the subsurface remote sensing curves. Good retrieval of OP's and water depths, which play a very important role in determining the appropriate abundances for purposes of benthic mapping. In the past chapter, the CIUB approach showed to have very close estimated parameters with those already validated by Goodman, and even better performance in water depth estimation as compared with SHOALS data.

Bottom composition estimates were very similar to those obtained by Goodman. The shore area obtained algae estimates that compare with Goodman's. Small spots of coral were also similar located in the center of the bay, and probably the CIUB estimated more coral than Goodman, especially in the center region.

# Chapter 6

# Conclusions and Future Work

## 6.1 Conclusions

The main purpose of this study was to provide the remote sensing community with new tools for making easier the process of retrieving bathymetry and benthic composition of coastal areas. This work provides with a new algorithm that efficiently retrieve optical properties and provides reasonable estimates of benthic composition (an approximation of the bottom surface), optical properties of the water column and water depth estimates. The innovation of this method is that it takes advantage of the high spectral information of hyperspectral imagery to account for the estimation of both the optical properties and bathymetry obtained by Lee's inversion model while simultaneously providing estimates of benthic composition estimates, also considering for the water column effects. Also, it performs the abundance estimates at the bottom surface, while in the past they were obtained using the linear mixing model at the water surface.

Two approaches that looked for improving the existing methods were tested with real and synthetic data. The method that implements a linear mixing model at the bottom surface (CIUB) proved to be more accurate than methods that perform unmixing at the water surface (CIUS, LIGU). Also, abundance estimates obtained were very similar to those obtained in [1], thus showing reasonable consistency in the benthic mapping of the

Kaneohe Bay. We may highlight a list of important assessments obtained with this research:

- For synthetic data, excellent retrieval of OP's and water depths up to 20 meters depth with good abundance estimates for up to 15-18 meters depth, assessed using the CIUB algorithm in simulated clear water. For optically dense water, the retrieval of OP's and water depth for up to 5 meters was attained with the CIUB. There is a tendency to estimate sand for water depths above those five meters.
- A fitting error in real data of about 20-30% is found for water depths above 10 meters, and sand is estimated for these same in both the validation dataset and the Kaneohe Bay image.
- Parameter G, although an optical property that describes the water column, shows its dependency on the bottom as seen with real data. Parameter P was constantly estimated to the same value (near or equal to 0.005), a lower bound for the optimization. This arises the question whether is necessary or not to include this parameter for retrieval, or just fixing it at a constant value.
- Fitting error accuracy for real pixels was very similar to those obtained by Lee's. A mean of 0.0239 and a variance of 5.865e-6 were obtained with the CIUB algorithm, compared to a 0.0239 and 5.7351e-6 (Lee's).
- Water depth estimates were very close to SHOALS measurements on pixels with 0.2 to 10 meters depth when dealing with real data. We applied linear regressions obtained a slope of 0.9806 and intercept of 0.2892 with the CIUB algorithm versus a 0.8891 and a 0.4694 using LIGU. Also, histograms that described the difference between the SHOALS data and the retrieved depths showed that the CIUB is superior, getting a mean of 0.3385 m and a variance of 2.336 m as compared to a mean -0.4030 m and 2.9698 meters variance for the LIGU.

## 6.2 Future Work

Several topics would be certainly useful to be studied:

- Sensitivity analysis on the inversion model.

This is to test how sensitive the estimates are to noise and depth in order to look for methods that deal with sensor noise and to improve our capability to estimate bottom composition at higher depths.

- Sensor fusion.

Available data like the SHOALS measurements would alleviate the problem of retrieving bathymetry, and possibly the optical properties and would certainly improve the capacity of the algorithm to retrieve benthic composition. This would also facilitate the analysis accuracy estimates of the other optical parameters.

- Incorporation of spectral libraries to the unmixing algorithm. This could help in more accurate mapping of the marine floor.

- Better understanding of mixing process. Mixing of bottom components under water is a nonlinear process.

- Look at regularized methods to deal with the problem of high sensitivity.

# References


[1] J.A. Goodman, S.L. Ustin, *Hyperspectral Remote Sensing of Coral Reefs: Deriving Bathymetry, Aquatic Optical Properties and a Benthic Spectral Unmixing Classification Using AVIRIS Data in the Hawaiian Islands*. Hydrologic Sciences Department, PhD Dissertation. Davis: University of California, 2004, pp. 74-135.

[2] M. Barreto, "*Implementation of a bio-optical model in IDL*". Electrical and Computer Engineering Department. M.E. Project. Mayagüez: University of Puerto Rico, 2004, pp. 1-45.

[3] "Inherent Optical Properties (IOPs)". Hydro-Optics, *Biology & Instrumentation Laboratories*, 2004. Web link: http://www.hobilabs.com/

[4] Zhong Ping Lee, Kendall L. Carder,Curtis D. Mobley,Robert G. Steward, Jennifer S. Patch, "Hyperspectral remote sensing for shallow waters: 2. Deriving bottom depths and water properties by optimization," in *Applied Optics*, vol. 38, 1999, pp. 3831-3843.

[5] Stéphane Maritorena, André Morel, Bernard Gentili, "Diffuse reflectance of oceanic shallow waters: Influence of water depth and bottom albedo," *Limnol. Oceanogr.* vol. 39, 1994, pp. 1689-1703.

[6] Heather Holden, Ellsworth LeDrew, "Optical Water Column Properties of a Coral Reef Environment: Towards Correction of Remotely Sensed Imagery". 0-7803-6359- IEEE. 2000, pp. 2666-2668.

[7] Davide D' Alimonte, Giuseppe Zibordi, Jean-Francois Berthon, "Determination of CDOM and NPPM absorption coeffient spectra from coastal water remote sensing reflectance," in *IEEE Transactions on Geoscience and Remote Sensing*, vol. 42, G. Zibordi, Ed., August ed., 2004, pp. 1770-1771.

[8] J.M. Anstee, A.G. Dekker,V.Brando,N. Pinnel,G.Byrne, P.Daniel,A. Held, "Hyperspectral imaging for benthic species recognition in shallow coastal waters," 0-7803-7031-1/01, IEEE. 2001, pp. 2513-2515.

[9] ZhongPing Lee, Kendall L. Carder, Curtiss O. Davis, "Using hyperspectral imaging to characterize the coastal environment," in *IEEE Aerospace Conference paper #472*, 2001.

[10] H. Loisel, P.Y. Deschamps, J.M. Nicolas,C. Moulin, "Polder-2/Ocean Color: ATBD Bio-optical Algorithms," *LOA*, Issue 5, 2002, pp. 3-7.

[11] Zhong Ping Lee, Kendall L. Carder,Curtis D. Mobley,Robert G. Steward, Jennifer S. Patch, "Hyperspectral remote sensing for shallow waters I. A semianalytical model," in *Applied Optics*, vol. 37, 1998, pp. 6329-6338.

[12] Zhong Ping Lee, Kendall L. Carder, Robert A. Amone, "Deriving inherent optical properties from water color: a multiband quasi-analytical algorithm for optically deep waters," in *Applied Optics*, vol. 4, 2002, pp. 5755-5772.

[13] Albert A., C.D. Mobley, "An analytical model for subsurface irradiance and remote sensing reflectance in deep and shallow case-2 waters," in *Optics Express*, vol. 11, 2003, pp. 2873-2890.

[14] Haigang Zhan, Zhong Ping Lee,Ping Shi, Chuqun Chen,Kendall L. Carder, "Retrieval of Water Optical Properties for Optically Deep Waters Using Genetic Algorithms," in *IEEE Transactions on Geoscience and Remote Sensing*, vol. 41, 2003, pp. 1123-1128.

[15] J.A. Goodman, S.L. Ustin, "Airborne hyperspectral analysis of coral ecosystems in the Hawaiian Islands," 2003.

[16] J. A. Cadzow, "Signal Processing via Least Squares Error Modeling," in *IEEE ASSP*, 1990.

[17] S. Rosario, M. Vélez, "Solving Abundance Estimation in Hyperspectral Unmixing as a Least Distance Problem". SPIE: Defense and Security Symposium ,Orlando, Florida, 2005.

[18] Hoeg-Guldberg, O. “Climate change, coral bleaching and the future of the world's coral reefs”. *Marine & Freshwater Research*, 1999, vol.50, pp. 839-866.

[19] Mumby P.J., Hedley J.D., Chisholm J.R.M. “The cover of living and dead corals from airborne remote sensing”. *Coral Reefs*. 2004, vol. 23, pp. 171-183.

[20] Purkis S.J., Pasterkamp R., “Integration in situ reef-top reflectance spectra with Landsat TM imagery to aid shallow-tropical benthic habitat mapping,” *Coral Reefs*. 2004, vol. 23, pp. 5-20.

[21] Smith R.B., *Introduction to Hyperspectral Imaging*. MicroImages, Inc. 2001, pp.1-24.

[22] Zhang Y., Pulliainen J.T., Koponene S.S., Hallikainen M.T., “Water Quality Retrievals From Combined Landsat TM Data and ERS-2 SAR Data in the Gulf of Finland,” *IEEE Transactions on Geoscience and Remote Sensing*, Vol. 42, NO. 3, March 2003, pp. 622-629.

[23] Mishra D.R., Narumalani S., Rundquist D., Lawson M., “High-Resolution Ocean Color Remote Sensing of Benthic Habitats: A Case Study at the Roatan Island, Honduras,” *IEEE Transactions on Geoscience and Remote Sensing*, Vol. 43, No.7, July 2005, pp. 1592-1604.

[24] Hunter, C.L., Evans, C.W., “Coral reefs in Kaneohe Bay, Hawaii: Two centuries of western influence and two decades of data,” *Bulletin of Marine Science*. March 1995, Vol. 57, no. 2, pp. 501-515.

[25] Leathers, R.A.; Downes, T.V.; Snyder, W.A., *Ocean PHILLS Data Collection and Processing: May 200 Deployment, Lee Stocking Island, Bahamas*. Naval Research Laboratory, NRL/FR/7212-02-10,010. February, 2002. pp. 30-34.

[26] K. L. Carder and R. G. Steward, “A remote-sensing reflectance model of a red tide dinoflagellate off West Florida,” *Limnol. Oceanogr.* 1985. 30, pp. 286–298.

[27] Kruse F.A. “Visible-Infrared Sensor and Case Studies”. *Remote Sensing for the Earth Sciences: Manual of Remote Sensing*, 3, 1999.

[28] Kruse F.A.; Boardman J.W.; Huntington J.F.; Mason P.; Quigley M.A. “Evaluation and Validation of EO-1 Hyperion for Geologic Mapping”. *IEEE International Geoscience and Remote Sensing Symposium,* 2002. 1. pp. 593- 595.

[29] Lawson C. L. and Hanson R. J. *Solving Least Square Problems*. Prentice-Hall, Inc., 1974.

[30] Rosario, S. “*Iterative Algorithms for Abundance Estimation on Unmixing of Hyperspectral Imagery”*. Master of Science Thesis, University of Puerto Rico at Mayagüez, May 2004.

[31] Jiménez Rodríguez, L.O. “Surface Object Recognition by Means of Regularization Techniques for Mapping Coastal Waters Floor”, Laboratory for

Applied Remote Sensing and Image Processing, University of Puerto Rico at Mayagüez, 2005.

[32] Adler Golden, S.M.; Acharya, P.K.; Berk, A.; Matthew, M.W. Gorodetzky, D., "Remote Bathymetry of the Littoral Zone From AVIRIS, LASH, and QuickBird Imagery", *IEEE Transactions on Geoscience and Remote Sensing*, Vol. 43, NO.2, February 2005. pp. 337-347.

[33] Irish, J., "An Introduction to Coastal Zone Mapping With Airborne Lidar: The SHOALS System". US Army Engineer Research and Development Center, Coastal and Hydraulics Laboratory, Joint Airborne Lidar Bathymetry Technical Center of Expertise. 2000.

[34] Davis, Curtis O.; Carder, Kendall L., "Using Hyperspectral Imagery to Characterize the Coastal Environment". *IEEE Aeronautics Conference*, paper #472, 2001. pp. 1515-1519.